Draft version August 11, 2020
Typeset using LaTeX **twocolumn** style in AASTeX63

The spectroscopic follow-up of the QUBRICS bright quasar survey

Konstantina Boutsia,[1] Andrea Grazian,[2] Giorgio Calderone,[3] Stefano Cristiani,[3,4,5] Guido Cupani,[3] Francesco Guarneri,[3,6] Fabio Fontanot,[3] Ricardo Amorin,[7,8] Valentina D'Odorico,[3,9,5] Emanuele Giallongo,[10] Mara Salvato,[11] Alessandro Omizzolo,[12,2] Michael Romano,[13,2] and Nicola Menci[10]

[1] *Las Campanas Observatory, Carnegie Observatories, Colina El Pino, Casilla 601, La Serena, Chile*
[2] *INAF–Osservatorio Astronomico di Padova, Vicolo dell'Osservatorio 5, I-35122, Padova, Italy*
[3] *INAF–Osservatorio Astronomico di Trieste, Via G.B. Tiepolo, 11, I-34143 Trieste, Italy*
[4] *INFN-National Institute for Nuclear Physics, via Valerio 2, I-34127 Trieste*
[5] *IFPU–Institute for Fundamental Physics of the Universe, via Beirut 2, I-34151 Trieste, Italy*
[6] *Dipartimento di Fisica, Sezione di Astronomia, Universit di Trieste, via G.B. Tiepolo 11, I-34131, Trieste, Italy*
[7] *Instituto de Investigación Multidisciplinar en Ciencia y Tecnología, Universidad de La Serena, Raul Bitrán 1305, La Serena, Chile*
[8] *Departamento de Física y Astronomía, Universidad de La Serena, Av. Juan Cisternas 1200 Norte, La Serena, Chile*
[9] *Scuola Normale Superiore, P.zza dei Cavalieri, I-56126 Pisa, Italy*
[10] *INAF–Osservatorio Astronomico di Roma, Via Frascati 33, I-00078, Monte Porzio Catone, Italy*
[11] *Max-Planck-Institut fr extraterrestrische Physik Giessenbachstrasse 1, Garching D-85748, Germany*
[12] *Specola Vaticana, Vatican Observatory, 00122 Vatican City State*
[13] *Dipartimento di Fisica e Astronomia, Università di Padova, Vicolo dell'Osservatorio 3, I-35122, Padova, Italy*

(Received April 20, 2020; Revised May 10, 2020; Accepted August 11, 2020)

Submitted to ApJS

ABSTRACT

We present the results of the spectroscopic follow up of the QUBRICS[a)] survey. The selection method is based on a machine learning approach applied to photometric catalogs, covering an area of $\sim$ 12,400 deg^2 in the Southern Hemisphere. The spectroscopic observations started in 2018 and identified 55 new, high-redshift ($z \geq 2.5$), bright ($i \leq 18$) QSOs, with the catalog published in late 2019. Here we report the current status of the survey, bringing the total number of bright QSOs at $z \geq 2.5$ identified by QUBRICS to 224. The success rate of the QUBRICS selection method, in its most recent training, is estimated to be 68%. The predominant contaminant turns out to be lower-z QSOs at $z < 2.5$. This survey provides a unique sample of bright QSOs at high-z available for a number of cosmological investigations. In particular, carrying out the redshift drift measurements (Sandage Test) in the Southern Hemisphere, using the HIRES spectrograph at the 39m ELT, appears to be possible with less than 2500 hours of observations spread over 30 targets in 25 years.

Keywords: quasars: general — catalogs — surveys, galaxies: nuclei

1. INTRODUCTION

Luminous quasars are the brightest non-transient cosmic beacons in the Universe. The hunt for such bright sources, especially at high redshift, is of paramount importance for a number of extragalactic studies, ranging from the number density of bright quasars at high-z (Schindler et al. 2019a), the theoretical modelling of the early phases of galaxy formation and co-evolution with their central SMBHs (e.g. Valiante et al. 2016; Fontanot et al. 2020), the study and characterisation of their (gas) accretion properties of the super massive black hole (SMBH) population (Wu et al. 2015; Wolf et al. 2018) to the inference on cosmological parameters from time delays of strongly lensed QSOs (Bonvin et al. 2017) and the properties of the dark matter by

Corresponding author: Konstantina Boutsia
kboutsia@carnegiescience.edu

[a)] Acronym for *"QUasars as BRIght beacons for Cosmology in the Southern hemisphere"*, (Calderone et al. 2019).

microlensing statistics in bright quasars (Webster et al. 1991; Bate et al. 2007).

Absorption signatures in the spectra of bright high-z QSOs are one of the most powerful and invaluable tools for studying intergalactic environments, as emerged from the recent Astro2020 Decadal Survey (e.g. Becker et al. 2019). Among the fundamental questions that can be tackled thanks to the study of QSO absorption lines we recall: the measurement of primordial Deuterium abundance (e.g. Cooke & Fumagalli 2018), the temperature evolution of the Cosmic Microwave Background (CMB), the free-streaming of warm dark matter (e.g. Iršič et al. 2017), the variation of the fundamental constants of nature, e.g. the fine structure constant or the proton-to-electron mass ratio (see Leite et al. 2016), the missing baryon problem (e.g. Werk et al. 2014), the production and diffusion of metals in the IGM (e.g. D'Odorico et al. 2016), the Lyman continuum escape fraction of high-z QSOs (e.g. Cristiani et al. 2016; Grazian et al. 2018), the mean free path of ionizing photons (e.g. Prochaska et al. 2009; Worseck et al. 2014; Romano et al. 2019), the reionization epochs of hydrogen and helium, and the sources responsible of these transition phases in cosmic history.

An appealing application of the detailed study of the Lyman forest in Cosmology is the so-called Sandage test (Sandage 1962), which can give fundamental constraints to General Relativity. The detection of the tiny drift due to cosmic expansion in the cosmological redshifts of many absorption lines in the spectra of bright QSOs will allow to measure directly cosmological parameters (e.g. Ω_M, Ω_Λ, H_0) at $2 < z < 5$ without the need of any local ladders or intermediate distance indicators. This revolution will be possible only with the brightest QSOs observed by the most powerful and stable high resolution spectrographs which will be available in the future at 20-40m telescopes (Liske et al. 2008).

However, finding the brightest quasars at high-z is not a trivial process. The advent of the SDSS survey (e.g. Fan & SDSS Collaboration 2000) represents a quantum leap in this respect, at least in the Northern hemisphere. At present, the SDSS has delivered more than 10^6 spectroscopically confirmed QSOs at $0 < z < 6.5$, with a large fraction at absolute magnitudes $M_{1450} \leq -26$. Recent studies, however, point out that, at very bright magnitudes, SDSS can suffer from incompleteness due to color selection (see also Fontanot et al. (2007)). For example, Schindler et al. (2019a) find 407 new bright QSOs at $2.8 < z < 5.0$ in the ELQ survey, showing that the SDSS completeness is $\sim 60\%$ at bright magnitudes ($i \leq 18$). As a consequence, the hunt for bright quasars, especially at high-z and in the Northern hemisphere, could be biased towards lower numbers due to the adoption of efficient but low completeness selections.

The situation is even more dramatic in the Southern hemisphere, due to the lack of wide multi-wavelength surveys at $\delta \leq 0°$ in the past. Comparing QSO surface densities, it is statistically evident that high-z objects of bright apparent magnitudes must be present also in the Southern hemisphere: of the 22 known QSOs with $z > 3$ and $V < 17$, only 5 are at $\delta < 0°$, and all the 3 QSOs with $V < 16$ are in the North (Véron-Cetty & Véron 2010).

In Calderone et al. (2019) (hereafter Paper I), we presented the first results of a survey of $z \geq 2.5$ QSOs at bright i-band magnitudes ($i \leq 18.0$) in the Southern hemisphere, taking advantage of the recent availability of new multiwavelength public databases. The combination of state-of-the-art databases with innovative techniques for the selection of the best candidates results in an efficient selection, with a success rate in finding high-z QSOs larger than 50% and a completeness in excess of 90%. In the first spectroscopic runs we already identified the intrinsically most luminous QSO at that time, with $z \geq 3.8$ at $\delta < 0°$, QSO J2157-3602, which has been afterwards independently confirmed by Schindler et al. (2019b). In this paper we will present a new z>4 QSO with apparent magnitude of $i = 16.886$ (see Section 4) that would be the new record holder in the Southern Hemisphere. In total we present 168 new bright QSOs at $z \geq 2.5$, thus quickly completing the identification of the high-z sample of Paper I.

The structure of this paper is the following: in Section 2 we summarize the selection method of our bright QSO candidate sample, in Section 3 and 4 we describe the massive observational campaign carried out at medium size telescopes and the spectroscopic identification of our QSO candidates. The properties of the newly identified high-z QSOs are discussed in Section 5, while Section 6 is devoted to the description of the Golden QSO sample for the Sandage test. Discussions and Conclusions are summarized in Section 7. Unless otherwise stated, apparent magnitudes are in the AB photometric system.

2. SELECTION METHOD

In this section we will describe the QUasars as BRIght beacons for Cosmology in the Southern hemisphere (QUBRICS) survey, first introduced in Paper I. We refer the reader to this work for more details of the method, while here we just recall its main characteristics.

To identify new, high-z QSOs candidates in the remaining sample, a classification algorithm has been applied based on the Canonical Correlation Analysis, (CCA, Anderson 1984). Our candidate list has been

drawn from a multiwavelength catalogue. We used the public databases of: i) Skymapper (DR1.1, Wolf et al. (2018)); ii) Gaia (DR2, Gaia Collaboration et al. (2018)); iii) 2MASS (Skrutskie et al. 2006) and iv) the WISE survey (Wright et al. 2010) to build the initial *main sample* (1014875 sources), covering ~ 12400 deg^2, with i-band magnitudes in the range $14 < m_i \leq 18$. The sources with secure object-type identification have been used as a training set and the recipe has been applied to the remaining sources in order to predict a likely classification. By using the parallax and proper motion estimates provided by Gaia, $\sim 83\%$ of the sources were classified as *bona fide* stars. Matching the remaining sources against the following catalogs: SDSS DR14Q (Pâris et al. 2018), Veron-Cetty QSO 13th edition (Véron-Cetty & Véron 2010), and 2dFGRS (Colless et al. 2001), led to reliably identify an object-type classification to 4666 QSOs and 3665 galaxies (in the following, the *original training set*). To discriminate against low-z (< 2.5) QSOs, we use the CCA as a regression algorithm to the objects classified as QSOs, in the previous step, to obtain an estimate of their redshift. In Paper I we tested this methodology with a resulting sample of 1476 candidates without spectroscopic confirmation, and our spectroscopic follow-up identified 54 QSOs with $z \geq 2.5$.

As the main focus of our work is the identification of the largest possible number of bright high-z QSO in the Southern Emisphere, we aim at the highest possible success rate of observing runs. Therefore, after each run we update the training set of the algorithm by including the new identifications: this results in an evolving list of QSO candidates. For the statistical purposes of this paper, the list of candidates has been frozen to its current form after the last observing run in Feb. 2020. At this point the list included 1412 sources in total, with 594 secure spectroscopic identifications and 818 candidates yet to be observed. Thanks to the revised training set it has been possible to reduce the number of candidates yet to be observed by $\sim 25\%$ with respect to the original list of Paper I. Fig. 1 and 2 illustrate the process of classification and redshift estimate, respectively, in the present work. They update the corresponding plots of Paper I.

It should be noted that the selection criteria adopted here and in Paper I could be biased against lensed sources. To reduce the contamination we have adopted relative stringent criteria about the positional coincidence in the various photometric catalogs. While this is not affecting "normal" QSOs, may have the subtle effect of removing lensed sources, forming extended structures like Einstein rings or crosses. Moreover, due to the choice of the fundamental photometric bands (e.g. GAIA), our selections is probably biased against sources at $z \gtrsim 4.5$.

3. SPECTROSCOPY

The QUBRICS pilot campaign has been presented in Paper I. Observations have been obtained using various instruments at Las Campanas Observatory (LCO), the TNG telescope, and the ESO-NTT telescope at La Silla. Between August 2019 and February 2020, we have been awarded more nights at these facilities, in order to expand our spectroscopic survey. We discuss here the details of these observations.

3.1. *WFCCD at duPont*

We have been awarded a total of 12 nights with the Wide Field CCD camera at duPont. We used the same configuration as in the pilot study, namely, the blue grism, with the 1.5" long slit, that covers a wavelength range between 3700 - 8000 Å giving a 2 Å/pixel dispersion. In total we have observed 100 candidates, but only 76 of them have a robust spectroscopic classification (flag=A). Of the securely classified sources, 63 (83%) are QSOs, and 36 of those (57%) are in the desired redshift range (z≥2.5).

3.2. *LDSS-3 at Clay*

A total of 44 candidates have been observed with LDSS-3 at the Clay telescope. Observations were obtained in several nights during bright time and variable weather conditions. We have used the VPH-all grism with the 1" - central slit and no blocking filter, covering a wavelength range between 4000 - 10000 Å with a low resolution of R∼800. Exposure times were ranging between 800 - 1800sec, depending on the candidate magnitude. Out of the observed candidates, 40 have a high quality redshift flag (flag A) and have been securely classified, most of them as QSOs (28 out of 40, 70%) but only 12 (43%) have a redshift above 2.5.

3.3. *EFOSC2 at NTT*

In September 2019 we were awarded three more nights (PI. A. Grazian, proposal 0103.A-0746) at NTT, to use the EFOSC2 instrument. In order to complete the survey, we obtained 4 additional nights at NTT in January 2020 (PI. A Grazian, proposal 0104.A-0754). Again, we used grism #13 (wavelength range $\lambda \sim 3700 - 9300$ Å), with typical exposure times ranging between 300 and 600 seconds. We observed 217 candidates, obtaining robust identification for 187. Out of these, 161 (86%) were classified as QSOs and 122 have a redshift of $z \geq 2.5$ (76%). This was one of the most efficient runs in this period.

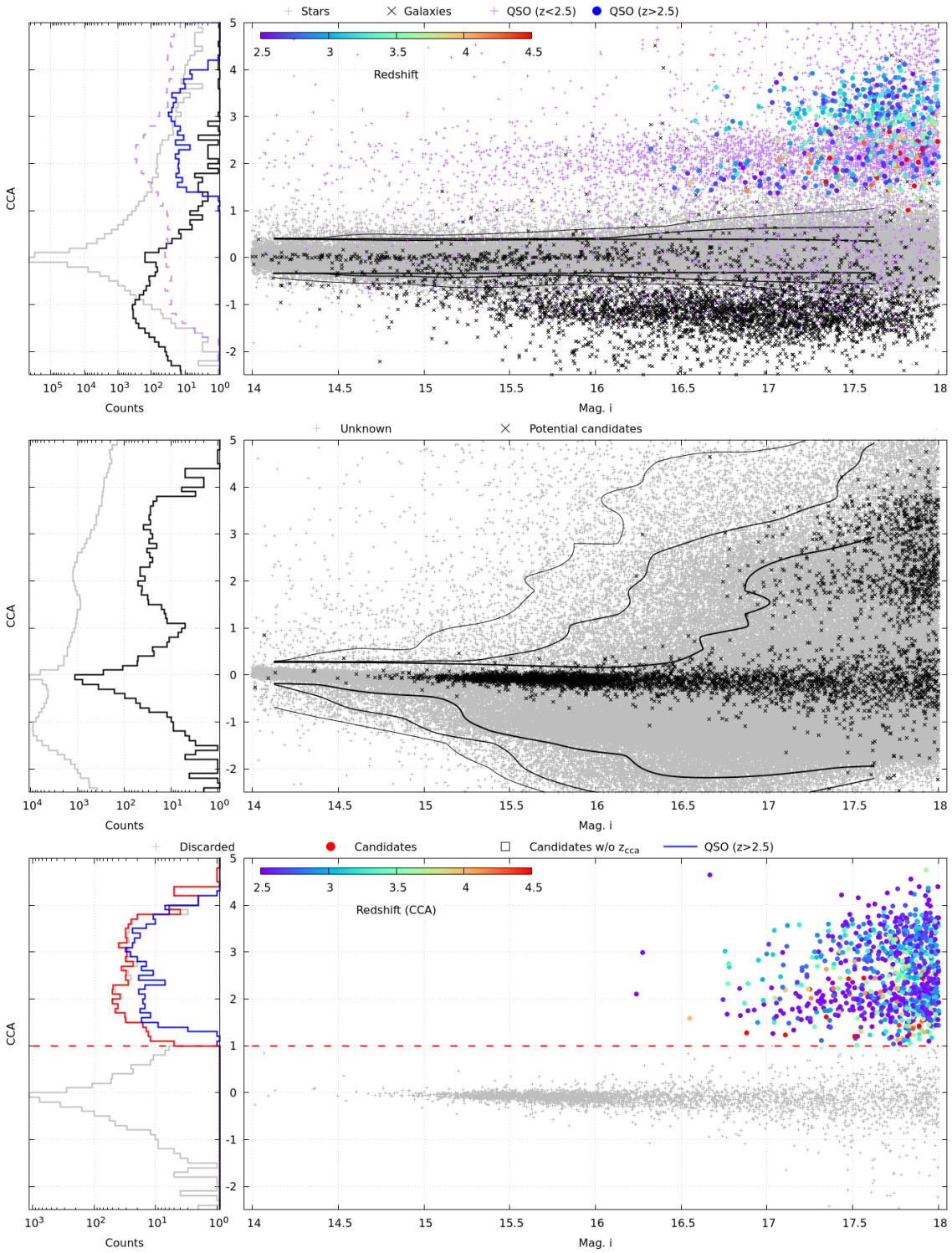

Figure 1. The `CCA`–i plane for the various subsamples considered in this work. For the statistical meaning of the CCA parameter shown in the y-axis we refer the reader to Paper I. Upper panel: sources in the *main* sample for which a reliable type identification is available. Stars are identified by gray "+" symbols, inactive galaxies by black cross symbols, low-z (< 2.5) QSOs with purple "+" symbols, high-z (≥ 2.5) QSOs with filled circles. The redshifts for the spectroscopically confirmed QSOs with $z \geq 2.5$ are shown with the color code shown in the colorbox in the upper left corner. The inset on the left shows the histogram of the `CCA` coordinate for the stars (gray), galaxies (black), low-z QSOs (purple) and known high-z QSOs (blue). Middle panel: sources in the *main sample* without an object type identification (gray symbols). The same sources after excluding extended and low-z objects are highlighted in black, and represents potential high-z QSO candidates. Lower panel: the *final* sample of high-z QSO candidates, with their redshift $z_{\rm cca}$ as in Paper I. The red dashed line represents the cut in the CCA selection. Candidates/observed sources are represented with open and filled circles respectively. The gray histogram represents the potential candidates, while the red and blue ones represent the QSO candidates and the confirmed QSO samples.

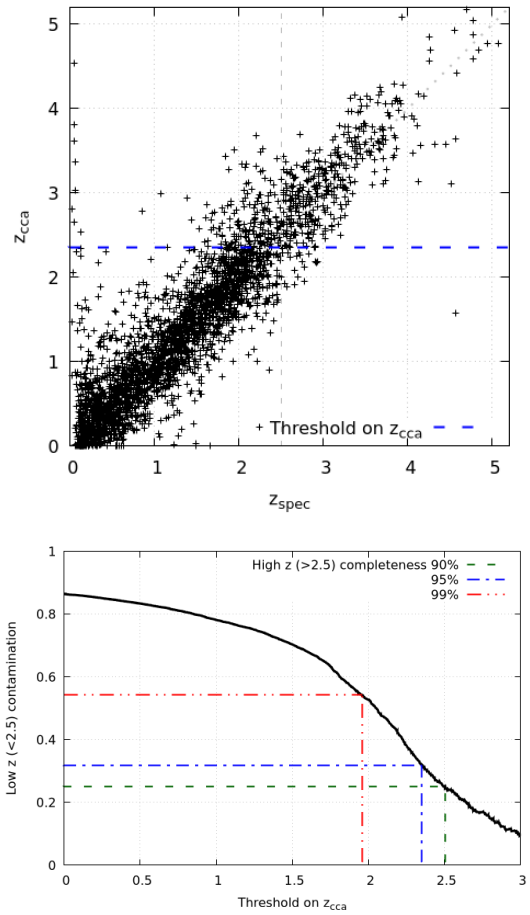

Figure 2. Upper panel: The $z_{\rm cca}$–$z_{\rm spec}$ correlation (scatter: ~ 0.37). The horizontal blue line is the threshold on $z_{\rm cca} = 2.26$, corresponding to a completeness of 95% and a contamination of 38%. Lower panel: contamination and completeness as a function of the threshold on $z_{\rm cca}$.

The outcome of this new spectroscopic campaign shows that, although our criteria are very efficient at identifying QSOs (84% of robust classifications are QSOs), only 55% are in the targeted redshift range. Anyhow, as discussed in Section 2, by ingesting the new QSOs to the selection algorithm, the efficiency of the selection for future spectroscopy is expected to be as high as 75% in the global sample.

3.4. *Data Reduction*

WFCCD data were reduced using standard IRAF tasks. After subtracting bias and dividing with flat, individual exposures were combined to the final image. We then used the task *apall* to extract the spectra and standard and *sensfunc* to calibrate in flux. The EFOSC2 and LDSS-3 spectra have been reduced with a custom pipeline using MIDAS scripts. The standard pre-reduction (i.e. bias subtraction and flat field normalization) has been adopted, and the wavelength calibration with helium, neon, and argon lamp has been obtained. We also check our wavelength solution on the emission night sky. An rms of 0.5 Å has been obtained from the wavelength calibration process. For WFCCD, EFOSC2 and LDSS-3, we made sure to obtain at least one spectro-photometric standard star per night. Since conditions have not always been photometric, the derived flux calibration is relative. There has been no further attempt to interpolate flux to known broad band magnitudes for absolute flux calibration. Further details can be found in Paper I. Improved data reduction of 3 objects observed in the runs of Paper I allowed us to upgrade their redshift flag to A. They are listed in Tab.4 with an appropriate identification in footnote.

3.5. *Redshifts from other surveys*

We have also searched the databases in the literature for additional reliable spectra of our candidates, finding 24 QSOs (6 with $z \geq 2.5$) and 1 AGN. They are listed in Tab. 1. In particular we found that downloading and analyzing spectra from the 6dF survey (Jones et al. 2009) we could assign a reliable redshift to 22 of our candidates. The candidate with SkyMapper ID 5578462 has spectral data of good quality in the ESO archive (see Fig. 3) that we have reprocessed. For the candidate with ID 10779504 we found a reliable redshift determination in the OzDES survey (Tie et al. 2017).

4. RESULTS OF THE SPECTROSCOPY

After 26 observing runs (including those reported in Paper I) we have collected the spectra of 511 sources, and 432 of them have a secure object-type classification. In total we identified 224 new bright QSOs at $z \geq 2.5$ (of which 15 at $z > 4$), 166 QSOs/AGN at $z < 2.5$, 11 inactive galaxies and 31 stars. Among the observed sources, a small fraction has uncertain classification and/or redshift estimate. These sources have been assigned a flagB for a variety of reasons. More precisely 32% have flat spectra without clear emission features that could be either stars or galaxies. Another 68% have a tentative QSOs classification, but it is not possible to robustly estimate the redshift since there is only one emission line or they show broad absorption features that are difficult to interpret. Such sources will be the subject of additional observations in different wavelength ranges aiming to discover additional features that could facilitate classification. An example of such follow-up can be seen in Section 4.3.

The list of the 303 new sources, to be added to those reported in Paper I, and their basic properties are shown in Tab. 4.

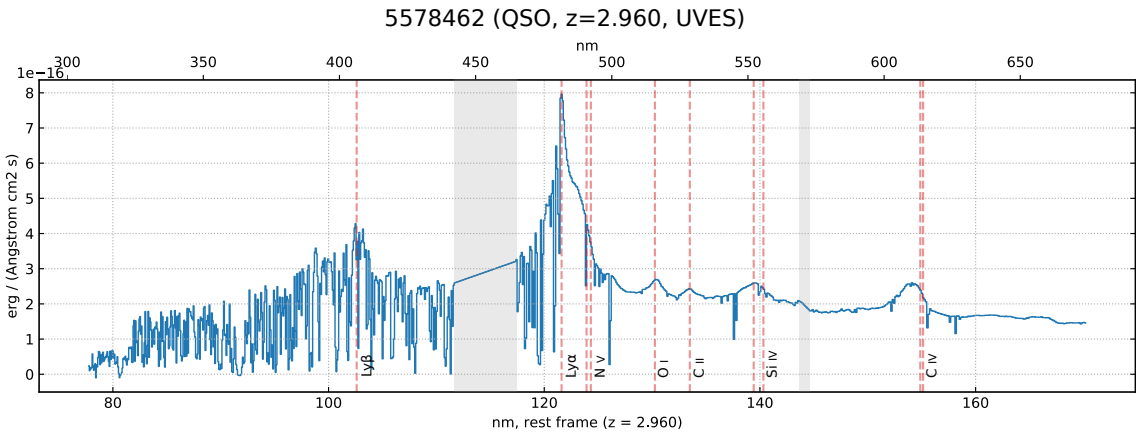

Figure 3. Composite UVES spectrum of a candidate at z=2.960, with some AGN emission lines highlighted. The grey bands are gaps in the UVES wavelength coverage, depending on the adopted instrument setup.

Table 1. Additional identifications from the literature.

Skymapper ID	R.A. (J2000)	DEC. (J2000)	m_i (mag)	$z_{\rm spec}$	Class	Survey
8414380	00:43:23.42	-00:15:52.5	17.781	1.442	QSO	6dF
8133493	00:44:48.56	-13:39:13.0	17.664	2.253	QSO	6dF
7885395	00:58:20.54	-19:04:03.2	17.983	1.861	QSO	6dF
9164524	02:03:03.20	-07:06:04.7	17.839	1.458	QSO	6dF
8826213	02:08:41.52	-19:44:03.7	17.943	2.137	QSO	6dF
8970643	02:29:45.41	-18:17:11.5	17.246	1.817	QSO	6dF
315606464	03:06:13.56	-57:51:05.3	17.925	2.066	QSO	6dF
318330107	03:14:59.84	-45:45:28.6	17.967	2.198	QSO	6dF
10372687	03:26:13.41	-31:00:52.2	17.869	2.105	QSO	6dF
10779504	03:39:53.34	-27:00:53.4	17.988	2.410	QSO	DES
10460382	03:40:42.83	-34:00:44.3	17.800	1.944	QSO	6dF
10812487	03:47:14.85	-24:38:08.7	17.427	3.130	QSO	6dF
11616376	04:22:43.67	-29:25:29.9	17.767	2.529	QSO	6dF
12053071	05:05:55.83	-29:30:38.5	17.865	1.070	QSO	6dF
56866269	10:18:21.75	-21:40:07.8	17.547	2.441	QSO	6dF
57772960	11:18:10.70	-17:51:59.3	15.119	0.215	AGN	6dF
63944442	12:12:18.99	-25:47:26.1	17.620	2.532	QSO	6dF
65530384	12:28:48.22	-01:04:14.7	17.039	2.642	QSO	6dF
64459508	12:31:32.96	-14:36:30.9	16.888	2.418	QSO	6dF
65808873	13:25:09.61	-08:04:48.2	17.786	2.359	QSO	6dF
308760834	22:21:10.25	-44:31:57.3	17.501	2.071	QSO	6dF
1459087	23:06:37.40	-36:49:26.0	17.962	2.650	QSO	6dF
308911502	23:21:22.33	-50:28:17.5	17.701	2.297	QSO	6dF
5578462	23:21:28.67	-10:51:22.3	17.769	2.958	QSO	ESO

The success rate, defined as the fraction of high-z QSOs among all the sources with a secure classification, as selected by our algorithm (§2), is relatively high (412 / 726 = 57%) for the old Paper I list and 405 / 594 $\sim$ 68% for the present work. The main contaminant (in the case of the present work the only one) is represented by low-z ($z < 2.5$) QSOs/AGNs. If we consider only the 1412 selected sources as described in Sect. 2, 266 have been observed and 199 turned out to be $z \geq 2.5$ QSOs, corresponding to a success rate of 75%.

In the present work, the success rate could be biased towards higher values, due to the self-learning approach described in Section 2. If we consider the effective success rate, i.e. the global ratio of high-z QSOs identifications carried out by us over all spectroscopic observa-

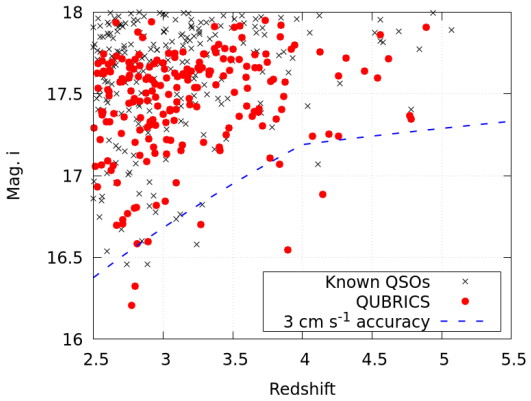

Figure 4. The redshift-i magnitude plane of the QSOs in the area of the present survey. Black crosses: QSOs known before the present observations; Red filled circles: new spectroscopic redshifts obtained in QUBRICS. The dashed blue line shows, in the context of the Sandage Test, the locus of an accuracy of 3 cm/s in radial velocity, reachable allocating 2500 h of observations at the ELT to a single QSO (see Sect. 6 for details).

tions done so far, including empirical attempts on improbable candidates, we still obtain a remarkable 52%.

All machine learning algorithms are biased by the features of the initial input sample. In this survey, the initial training set has been created based on all known spectroscopically confirmed QSOs from the literature, selected with a wide range of methods. Thus, bias towards specific types of sources should be minimal. However, in order to better assess the properties of our (evolving) selections and achieve a better training, we have carried out observations also of some objects not complying with our initial specifications, for example with no GAIA counterpart within the established radius or not point-like according to our criteria or fainter than 18mag in the i band ($i > 18$), thus not included in the Main Sample. These objects are also listed in Tab. 4 which contains two columns to show whether the object is a candidate according to the criteria of Paper I or/and selected according to the present work. Sources not included in the Main Sample are indicated with asterisks.

The total number of QSOs with $z \geq 2.5$ (and $i \leq 18$) in the QUBRICS *main sample* is 428, with 202 discovered by our survey and 226 sources derived from the literature. The machine learning algorithm applied in Paper I was able to identify 412 of the 428 $z \geq 2.5$ known QSOs (96%). Following the self-learning approach, i.e. by re-ingesting all new identifications in the training set, this completeness indicator becomes $405/428 = 95\%$.

4.1. *QSOs at $z \geq 2.5$*

Tab. 4 lists 168 new bright QSOs with spectroscopic redshift z≥2.5, and considering the sources already published in PaperI, the total number of new bright QSOs discovered by our survey amounts to 224.

Fig.4 shows the updated redshift-magnitude diagram for $z \geq 2.5$ quasars in the area of the QUBRICS survey. Red points indicate sources published in Paper I or here. Out of the 10 new QSOs at $z \geq 4.0$ the brightest is 316292063 with a z=4.147 and m_i=16.88, shown in Fig. 5. As seen in the figure, this QSO has rather narrow lines and this could perhaps indicate a type2 QSO or a lensed source. Additional observations have already been requested and its spectrum will be discussed in detail once our follow-up is completed. Our list includes 5 sources that were already published by Wolf et al. (2020) and were independently selected and classified by our survey.

4.2. *QSOs at $z < 2.5$*

Out of the 121 sources with flag A that are not high-z QSOs, there are 25 with redshift $z \leq 0.5$ and 78 QSOs at $0.5 < z < 2.5$. Thus 85% of the sources (103 out of 121) are active galaxies, but not in our desired redshift range. These relatively bright objects may still turn out to be useful for studies of the evolution of the metal content of the IGM, and of the Lyman forest at low redshift with space observations.

4.3. *Notes on BAL QSOs*

Both in the pilot and the main campaign, we have encountered sources with pronounced absorption troughs whose classifications, due to the lack of strong emission lines, is not straightforward. A fraction of these sources can in fact be classified as Overlapping Iron Low-ionisation BAL QSOs or OFeLoBAL (Hazard et al. 1987). OFeLoBALs are characterized by extensive systems of low ionization absorption which sometimes appear as broad saturated troughs (e.g. Hall et al. 2002). The troughs may overlap to nearly completely absorb the continuum emission shortward of 2800 Å, effectively mimicking the appearance of the Lyman forest. The estimated fraction of OFeLoBAL QSOs is around 2% (Dai et al. 2012) and their number in our catalogue can be as high as the number of genuine $z > 4$ QSOs.

The nature of these sources can be confirmed by identifying the Balmer series in the AGN emission, and in particular the Hα emission line at 6563 Å rest-frame. For $z \gtrsim 0.5$ this line is observed in the NIR band. We thus obtained NIR spectroscopic data for some of these sources, using the Folded-port InfraRed Echellete (FIRE), at the Baade Magellan telescope, with a long-slit configuration.

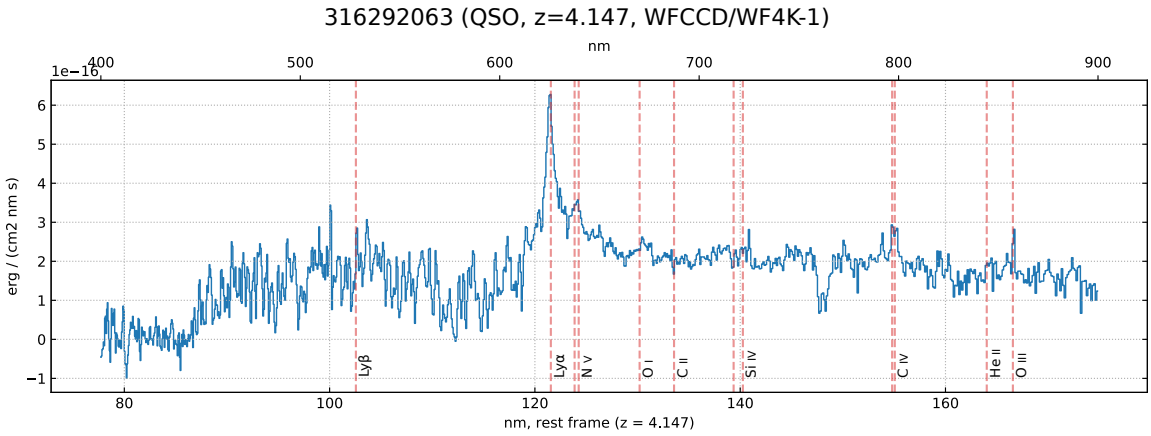

Figure 5. Spectrum, resampled at 250 km/s, of the brightest z∼4 QSO in the sample, with some AGN emission lines

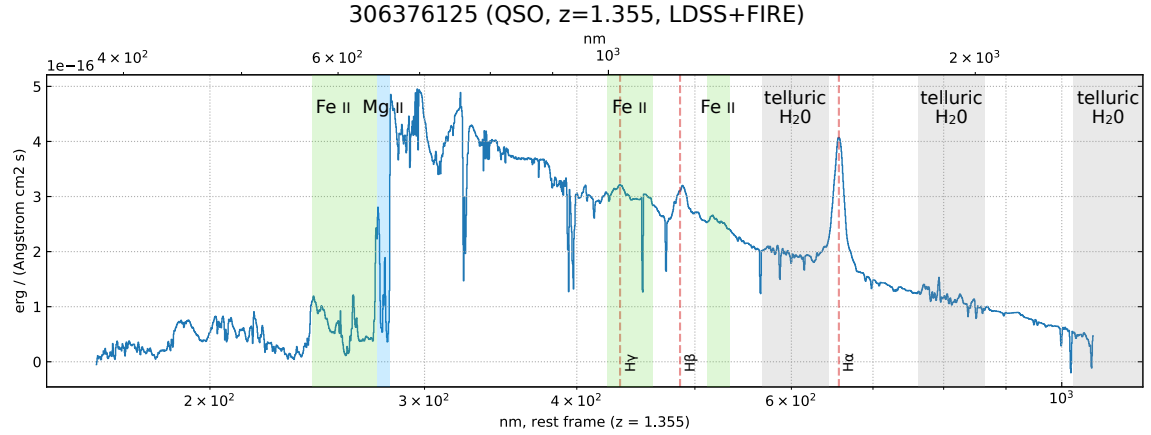

Figure 6. Spectrum, resampled at 250 km/s, of a candidate identified as an OFeLoBAL QSO, with some spectral features highlighted. AGN emission lines and metal bands are shown in color, while telluric bands (which have been corrected for in data reduction) are shown in grey.

A composite LDSS-3/FIRE spectrum of one such source (Skymapper ID 306376125), flux-calibrated in the visual band using an additional low-resolution spectrum taken by the Magellan Echellette Spectrograph (MagE) at Baade, is shown in figure 6. For this particular object, the Hα and Hβ line are clearly identified at $z = 1.355 \pm 0.001$, with the possible additional detection of Hγ blended within a Fe II emission complex. An overlapping Fe II-Mg II absorption complex at the same redshift is also clearly observed around 2600-2800 Å rest-frame, corroborating the identification of the candidate as a OFeLoBAL QSO. A detailed analysis of this object and of other similar sources (currently assigned a flagB classification and not included in Tab.4), is beyond the scope of this work, and will be discussed ' in a future publication.

5. PROPERTIES OF CONFIRMED QSOS

5.1. *IR colors*

Several recent surveys targeting super bright high-redshift QSOs are using WISE colors for the selection (Wolf et al. 2018; Schindler et al. 2019b; Wang et al. 2016). Based on a study by Wu et al. (2012), WISE colors are very good at distinguishing QSOs from late-type stars and more than half of SDSS QSOs have $W1-W2 > 0.57$. Wang et al. (2016) showed that high redshift QSOs, $z > 4.5$, are within the $0 < (W1 - W2) < 1.5$ color range. This has also been confirmed by the survey conducted by Wolf et al. (2018). In Fig.7 we show the distribution of our confirmed QSO candidates in the color space used by Wolf et al. (2018). In that work they were only interested in $z > 4.5$ QSOs, but in our sample we have a wide range of redshifts going from $2.5 \leq z < 5.0$. In order to be able to directly compare our distributions with the aforementioned works in the literature, presented WISE colors are in Vega magnitudes.

As can be seen in our plots, while all our candidates are indeed within the W1-W2[0,2] range, based only on

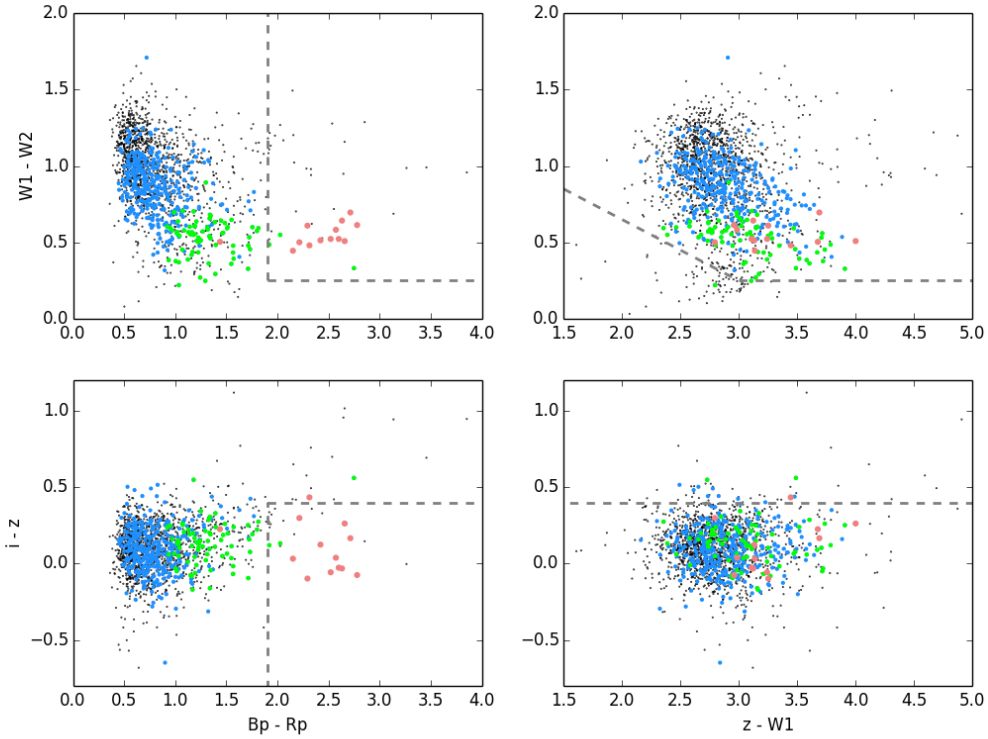

Figure 7. Color-color diagrams of all candidates with known redshift. Blue symbols are sources with $z \geq 2.5$, green with $z \geq 3.5$ and red with $z \geq 4.5$. The lines correspond to cuts similar to the ones applied by Wolf et al. (2020) to select high redshift bright QSOs ($z \geq 4.5$). The area delimited by the cuts is where the majority of $z \geq 4.5$ sources are found. WISE magnitudes are in Vega and the rest are in the AB system.

IR colors it is difficult to distinguish between the various redshifts, since all sources are mixed in a small area. Instead, when we include the GAIA ($B_p - R_p$) color, the redshift groups are better separated as seen in the two panels on the left of the figure. Most of our $z \geq 4.5$ confirmed QSOs have a color of $B_p - R_p$ >1.9, in line with the Wolf et al. (2018) selection. In addition, all $z \geq 2.5$ QSOs have a color $B_p - R_p$ >0.5, with the $z \geq 3.5$ source predominantly being in the area above $B_p - R_p$ =1.0. Thus, including bluer colors in the selection, can help to better target higher redshift sources.

5.2. *Crossmatch to Galex*

We have cross-matched the QSOs found in QUBRICS with the catalogs of the sources detected by GALEX[1] (Bianchi et al. 2017). Of the 414 QSOs/AGN confirmed in Paper I and II (including those from table 1) we have 161 detections with a confidence level > 2σ in the NUV and 83 detections in the FUV; 75 objects are detected both in the FUV and NUV. If we consider only QSOs with $z \geq 2.5$ ($z \geq 3.5$) out of 230 (54) objects 38 (3) have been detected in the NUV, 17 (2) in the FUV and 13 (1) both in the FUV and NUV.

In the designing phase of the QUBRICS we decided against using GALEX data for the selection of the candidates in order to avoid undesired selection effects relative to the fluctuations in the galactic absorption, which are stronger at UV wavelengths. In fact, we plan to use the QUBRICS sample to study the HeII reionization and the cosmic UV background. In order to fulfill this goal, we need an unbiased sampling of all the possible lines-of-sight in our QSO catalogue and a UV selection may select preferentially less absorbed ones (e.g. Prochaska et al. (2009)), which might bias future results towards shorter mean free paths in the IGM (Romano et al. 2019).

Indeed, one of the QSOs confirmed in Paper I, J045011.37-432429.7, with $z = 3.95$, shows a detection in the FUV and a non-detection in the NUV. FUV-loud QSOs are extremely rare at $z > 3.5$ and precious to study the He II reionization (Worseck et al. 2019).

[1] All the GALEX data used in this section can be found in MAST: https://doi:10.17909/T9H59D.

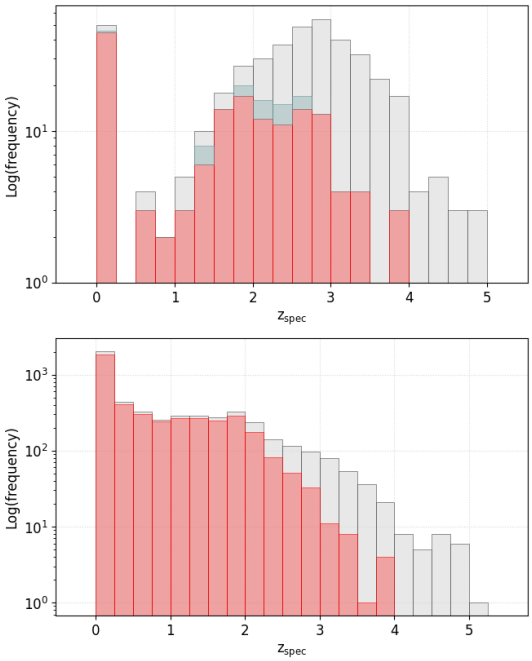

Figure 8. Upper panel: redshift distribution of the 414 confirmed QSOs/AGN (grey columns): 169 of those have a corresponding GALEX source in FUV, NUV or both. 152 of them (red columns) were observed by us, while the remaining 17 sources (light blue columns) were found in the literature (§3.5). Lower panel: redshift distribution of QSOs/AGN in the QUBRICS *main sample*. Grey columns show the distribution for all the objects, red columns for those with a GALEX counterpart.

J045011.37-432429.7 is potentially a case of transmission peaks that might indicate an example of patchy reionization of He II at $z \gtrsim 3.5$.

As shown in Fig. 8, all of QSOs/AGN with a GALEX counterpart have $z < 4$, J045011.37-432429.7 being the object with the highest recorded redshift. Moreover, considering the confirmed QSOs/AGN in paper I and II, 82% of objects below $z = 2$ have a GALEX counterpart. This number decreases drastically when considering higher redshift intervals: for $2 < z < 3$ ($3 < z < 4$) 35% (11%) of QSOs have a corresponding GALEX source. Similar results are obtained using all the QSOs/AGN known in the QUBRICS *main sample*, the biggest difference being for $2 < z < 3$ where a higher percentage (58%) of sources have a GALEX counterpart. In principle, the GALEX detection can be used as a veto criterium to increase the efficiency in the selection of bright QSOs at $z > 4$.

6. A GOLDEN SAMPLE FOR THE SANDAGE TEST

The redshifts of all cosmologically distant sources are expected to experience a small, systematic drift as a function of time due to the evolution of the expansion rate of the Universe (Sandage 1962). Liske et al. (2008), using extensive Monte Carlo simulations, determined the accuracy with which the redshift drift can be measured from the Lyman forest (and metal lines), σ_v, as a function of signal-to-noise ratio and redshift:

$$\sigma_v = g{\times}1.35 \left(\frac{S/N}{3350}\right)^{-1} \left(\frac{1+z_{\rm QSO}}{5}\right)^{-\gamma} \left(\frac{N_{\rm QSO}}{30}\right)^{-0.5} \text{cm/s} \quad (1)$$

where the symbol 'S/N' refers to the total S/N per 0.0125 Å pixel per object accumulated over all observations, $N_{\rm QSO}$ is the number of QSOs in the sample, $z_{\rm QSO}$ is the redshift of the QSO, the γ exponent is 1.7 for $z_{\rm QSO} \leq 4$ and 0.9 above. The form factor g is equal to 1 if all the targets are observed twice, at the beginning and at the end of the experiment, and becomes larger if the measurements are distributed in time, reaching 1.7 for a uniform distribution. The S/N per pixel for photon-noise limited observations can be written as:

$$S/N = 650 \left[\frac{Z_X}{Z_r}\, 10^{0.4(16-m_X)} \left(\frac{D}{39\text{m}}\right)^2 \frac{t_{\rm int}}{10h}\, \frac{\epsilon}{0.25}\right]^{\frac{1}{2}} \quad (2)$$

where D, $t_{\rm int}$ and ϵ are the telescope diameter, total integration time and total efficiency, Z_X and m_X are the zeropoint and apparent magnitude of the source in the X-band, respectively, and $Z_r = (8.88 \times 10^{10})$ s^{-1} m^{-2} μm^{-1} is the AB zeropoint for an effective wavelength of 6170 Å [corresponding to the Sloan Digital Sky Survey (SDSS) r-band]. The normalisation of the above equation assumes a pixel size of 0.0125 Å and a central obscuration of the telescope's primary collecting area of 10 per cent.

Liske et al. (2008) concluded that an ELT-type telescope (at the time planned with a 42m primary mirror) would be capable of unambiguously detecting the redshift drift over a period of $\sim$ 20 yr using 4000 h of observing time. The estimated amount of time would obviously increase assuming the 39m primary mirror of the ELT and considering only the QSOs observable with the ELT, typically those in the Southern hemisphere. We have repeated the estimate of the time requested to carry out the Sandage Test with the 39m ELT, adopting a strategy that maximizes the significance of the detection of a non zero redshift drift (Liske et al. 2008) (i.e. with QSOs in the redshift range $2.8 \leq z < 5$), aiming at a 3σ detection and observing 30 targets twice at 25 years distance. Other assumptions are the same as in Liske et al. (2008) except for the spectral slope of the QSO continuum, updated to be $f_\lambda \propto \lambda^{-1.3}$ (Cristiani et al.

Table 2. The golden sample of Southern QSOs for the Sandage Test

Name	R.A. (J2000)	DEC. (J2000)	m_r	m_i	G_{GAIA}	redshift	t(22.5 cm/s)	ID
	(deg)	(deg)	(mag)	(mag)	(mag)		(h)	Skymapper
J000322.94-260317.9	000.845639	-26.055083	17.472	17.071	17.6019	4.111	61.2	7437380
J000736.55-570151.8	001.902387	-57.031067	17.992	17.240	17.9440	4.260	70.5	317358346
J004131.41-493611.7	010.381000	-49.603247	16.736	16.580	16.7048	3.240	68.5	317850840
J010318.05-130509.9	015.825313	-13.086163	17.637	17.242	17.7349	4.072	71.9	8430815
J015558.26-192848.8	028.992816	-19.480298	17.673	17.393	17.7969	3.655	96.7	8789744
J015644.67-692216.1	029.186291	-69.371155	16.637	16.325	16.5949	2.800	78.7	314938059
J020413.26-325122.8	031.055213	-32.856350	17.276	17.068	17.3900	3.835	66.2	6932623
J030722.89-494548.2	046.845395	-49.763410	*	17.407	18.4534	4.728	78.8	318204033
J033015.31-543021.1	052.563812	-54.505886	17.203	17.174	17.2208	3.400	97.4	316834279
J042214.78-384452.9	065.561596	-38.748007	16.896	16.765	16.9504	3.123	84.2	10914737
J054803.19-484813.1	087.013348	-48.803654	17.215	16.886	17.2414	4.147	51.4	316292063
J093542.69-065118.8	143.927899	-06.855260	18.008	17.424	18.1236	4.040	85.3	56483517
J094253.51-110425.9	145.722949	-11.073870	16.915	16.733	16.8174	3.093	87.0	56438607
J101529.36-121314.3	153.872359	-12.220648	17.857	17.255	17.7070	4.190	72.0	57929040
J104856.82-163709.2	162.236717	-16.619244	17.194	17.164	17.2249	3.370	98.0	57339247
J105122.70-065047.8	162.844537	-06.846624	17.584	17.345	17.8003	3.765	88.1	58181076
J105449.68-171107.3	163.706991	-17.185386	17.104	17.107	17.2681	3.765	70.8	57368436
J111054.67-301129.8	167.727860	-30.191652	*	17.346	18.5117	4.780	74.2	54680559
J132029.98-052335.1	200.124872	-05.393160	17.559	17.444	17.8589	3.700	99.4	65911949
J144943.17-122717.5	222.429861	-12.454868	16.953	16.703	17.0963	3.273	82.3	66962683
J150527.83-204534.9	226.365934	-20.759752	16.966	16.955	16.9888	3.090	91.3	72002629
J162116.92-004250.8	245.320512	-00.714142	17.457	17.386	17.6713	3.703	94.1	114286192
J195302.67-381548.3	298.261202	-38.263482	17.724	17.305	17.8896	3.712	87.0	135100950
J200324.11-325145.0	300.850485	-32.862537	17.470	17.296	17.6287	3.783	83.6	135386798
J201741.49-281630.0	304.422893	-28.274988	17.822	17.388	17.7996	3.685	95.0	136198132
J212518.38-420547.6	321.326583	-42.096609	17.266	17.363	17.6598	3.549	98.8	307443251
J212540.96-171951.3	321.420690	-17.330947	16.644	16.548	16.8730	3.897	39.9	2379862
J212912.18-153840.9	322.300733	-15.644734	17.035	16.824	17.0243	3.280	88.4	2552049
J215228.21-444603.9	328.117538	-44.767760	17.310	17.291	17.3645	3.473	94.8	307536968
J215728.21-360215.1	329.367623	-36.037557	*	17.367	18.2864	4.771	75.7	397340

2016). For simplicity we have required that the spectra of all the objects are integrated for a sufficiently long exposure time (different for each target, depending on its magnitude and redshift) to reach the same velocity accuracy (22.8 cm/s) required for a global 3σ detection of the drift.

We collect in Tab. 2 our proposed sample of 30 Southern QSOs, most suitable for the Sandage Test. Thanks to the detection of new bright QSOs at high redshift, the total time required to carry out the Sandage Test turns out to be less than 2500 h and each QSO in Tab. 2 needs less than 100h of integration to provide a velocity accuracy of 22.8 cm/s.

7. DISCUSSION AND CONCLUSIONS

In this paper, we present spectroscopic identifications of QSO candidates in the QUBRICS sample, using our most updated selection criteria based on the CCA approach, which has been described in Paper I. At present, after 26 observing runs at intermediate and large telescopes (duPont, Magellan, NTT, TNG), we have been able to approximately double the number of bright QSOs ($i \leq 18.0$) at $z \geq 2.5$ known in the Southern Hemisphere, bringing it to 428. In this way it has been possible to relieve the persistent lack of bright targets for high resolution spectrographs of Southern observatories.

Using the new spectroscopic sample of bright QSOs from QUBRICS, we are able to further refine our selection criteria, by means of a new CCA training set. The completeness of the selection criterion, evaluated against the presently known bright QSOs at $z \geq 2.5$, turns out to be higher than 90%, while the success rate is around 70%. The success of the QUBRICS survey is particularly evident looking at Fig. 4, where among the new identifications we show the two brightest QSOs at $z \geq 3.8$ in the Southern hemisphere, with an increase of a factor of ~ 3 of the number of QSOs at $z \geq 3$ and $i \leq 17.5$.

The QUBRICS survey also selects rare and peculiar sources, with strong absorption features, e.g. the OFeLoBAL QSO discussed in section 4.3. With the progress of our survey it will be important to quantify

the number densities of these peculiar sources and to compare them with the relative low incidence in the past surveys.

Due to the characteristics of our selection, QUBRICS is expected to be incomplete for QSOs at $z \gtrsim 4.5$ or with images distorted by lensing. In the future, we will address these issues and try to reduce the biases with improved, less stringent selection criteria.

Surveys similar to QUBRICS have been started recently, based mainly on IR selections of bright high-z QSOs (e.g. Wolf et al. 2020; Schindler et al. 2019b). IR colors from 2MASS and WISE are fundamental to distinguish high-z QSOs from local galaxies or stars, but, taken alone, they are not optimal for a photometric redshift refinement. As discussed in Section 5, the optical colors $Bp-Rp$ or $i-z$ are very useful to separate QSOs at $z \sim 2$ from the ones at $z \sim 4$.

Besides, adopting further filters, in particular at short wavelengths (e.g. GALEX), it would be possible to further improve the success rate of the survey at high z. However, due to the possibility of introducing a bias against clear lines of sight in the intervening IGM, which can mimic the photometry of a lower redshift source (Romano et al. 2019), we chose not to use the GALEX photometry for the selection. In this way, among the newly discovered QSOs at $z > 2.5$, we have 29 objects with FUV or NUV detections, potentially important for follow up studies with COS for the HeII reionization (e.g. Worseck et al. 2016, 2019).

The adopted CCA method to compute a photometric redshift, described in Paper I, is based on SEDs extending from the u band to the WISE bands, and should be less affected by possible biases due to the presence of significant Lyman limit absorbers with short mean free paths, which are evident at $z \sim 3.5$ on QSO surveys based on $u-g$ color selections, as shown by Prochaska et al. (2009); Cristiani et al. (2016); Romano et al. (2019). In the future, we will address the effects of optical color selections on the QSO spectral properties and Lyman limit statistics.

The discovery of bright cosmic beacons is especially important for the study of the IGM at high-z. In particular, the QUBRICS survey provides a large sample of bright high-z QSOs for the Sandage Test with future 40 meter class telescopes. We estimate that at present, less than 2500 hours of observations in 25 years are needed with the ELT-HIRES to carry out the redshift drift measurement (Liske et al. 2008) at the precision required to have a 3σ detection of the cosmological signal. Before QUBRICS, the targets available in the Southern Hemisphere would have required, in the same metrics, about 4000 hours to accomplish this goal. QUBRICS, in a sense, contributes to a multi-million saving, considering the projected cost of a night at ELT ($\gtrsim$ 50 MEU or $\gtrsim$ 60 M$ at the assumed cost of 320 KEU for an ELT observing night and an average of 9 hours per night).

We are continuing the pursuit for the brightest cosmic beacons, exploring other innovative methods, with the main goal of giving a realistic possibility to execute the Sandage test, only dreamed of a few years ago.

ACKNOWLEDGMENTS

We thank Gabor Worseck for enlightening discussions.

This work is based on data products from observations made with ESO Telescopes at La Silla Paranal Observatory under ESO programmes ID 103.A-0746(A), 0103.A-0746(B), and 0104.A-0754(A).

The national facility capability for SkyMapper has been funded through ARC LIEF grant LE130100104 from the Australian Research Council, awarded to the University of Sydney, the Australian National University, Swinburne University of Technology, the University of Queensland, the University of Western Australia, the University of Melbourne, Curtin University of Technology, Monash University and the Australian Astronomical Observatory. SkyMapper is owned and operated by The Australian National University's Research School of Astronomy and Astrophysics. The survey data were processed and provided by the SkyMapper Team at ANU. The SkyMapper node of the All-Sky Virtual Observatory (ASVO) is hosted at the National Computational Infrastructure (NCI). Development and support the SkyMapper node of the ASVO has been funded in part by Astronomy Australia Limited (AAL) and the Australian Government through the Commonwealth's Education Investment Fund (EIF) and National Collaborative Research Infrastructure Strategy (NCRIS), particularly the National eResearch Collaboration Tools and Resources (NeCTAR) and the Australian National Data Service Projects (ANDS)

This work has made use of data from the European Space Agency (ESA) mission *Gaia* (https://www.cosmos.esa.int/gaia), processed by the *Gaia* Data Processing and Analysis Consortium (DPAC, https://www.cosmos.esa.int/web/gaia/dpac/consortium). Funding for the DPAC has been provided by national institutions, in particular the institutions participating in the *Gaia* Multilateral Agreement.

This publication makes use of data products from the Two Micron All Sky Survey, which is a joint project of the University of Massachusetts and the Infrared Processing and Analysis Center/California Institute of Technology, funded by the National Aeronautics and

Space Administration and the National Science Foundation

This publication makes use of data products from the Wide-field Infrared Survey Explorer, which is a joint project of the University of California, Los Angeles, and the Jet Propulsion Laboratory/California Institute of Technology, funded by the National Aeronautics and Space Administration.

This paper includes data gathered with the 6.5 meter Magellan Telescopes located at Las Campanas Observatory, Chile.

This research is based on observations made with the Galaxy Evolution Explorer, obtained from the MAST data archive at the Space Telescope Science Institute, which is operated by the Association of Universities for Research in Astronomy, Inc., under NASA contract NAS 526555.

We thank Società Astronomica Italiana (SAIt), Ennio Poretti, Gloria Andreuzzi, Marco Pedani, Vittoria Altomonte and Andrea Cama for the observation support at TNG. Part of the observations discussed in this work are based on observations made with the Italian Telescopio Nazionale Galileo (TNG) operated on the island of La Palma by the Fundacion Galileo Galilei of the INAF (Istituto Nazionale di Astrofisica) at the Spanish Observatorio del Roque de los Muchachos of the Instituto de Astrofisica de Canarias.

Facilities: Skymapper, Wise, 2MASS, Gaia, NTT (EFOSC2), Magellan:Baade (IMACS), Magellan:Clay (LDSS-3), Magellan:Baade (FIRE), du Pont (WFCCD), TNG (Dolores)

APPENDIX

A. CCA MATRIXES

Our QSO candidate selection procedure relies on a CCA transformation aimed at predicting an object type classification for each source, based on the photometric magnitudes in the bands where these estimates are available. In particular we associate a discrete numeric label to all sources with known object type classification, and search for the transformation matrix to be applied to the available magnitudes which maximizes the correlation with the above mentioned label. Note that the above process identifies the best possible linear transformation while the best performances would likely be obtained with a non-linear one, although the latter can not be obtained analytically. In order to improve our classification algorithm we also included the logarithm of each magnitude estimate in the CCA analysis. It should be noted that the availability of magnitude estimates is not the same for all the sources in our main sample, hence we identified 34 sub-samples with homogeneous availability and repeated the above process for each of them, resulting in 34 different CCA matrices. The largest sub-sample covers 43% of our main sample (438687 sources, with 58581 sources lacking a known object type classification). In Tab. 3 we report the transformation matrix used to calculate the CCA coordinate (i.e., the value displayed on the vertical axis of Fig. 1 in both Paper I and Paper II), for the above mentioned sub-sample.

All magnitudes should be converted to the AB system before applying the transformation, and an offset (last line of Tab. 3) should be added to the resulting label to obtain a classification on the same scale of the training. We can provide the matrices for the remaining sources on request.[2] Further details are available in Paper I.

Note that the presence of strong correlations among the magnitudes in different bands prevents us from drawing any conclusion by just comparing the numbers in the above matrices. The overall performance of each matrix, in terms of success rates and completeness, should thus be estimated by comparing the results with the test dataset, as discussed in §2.

REFERENCES

Anderson, T. 1984, An introduction to multivariate statistical analysis (Wiley Ed.)

Bate, N. F., Webster, R. L., & Wyithe, J. S. B. 2007, MNRAS, 381, 1591, doi: 10.1111/j.1365-2966.2007.12330.x

Becker, G., D'Aloisio, A., Davies, F. B., Hennawi, J. F., & Simcoe, R. A. 2019, BAAS, 51, 440. https://arxiv.org/abs/1903.05199

[2] Please write to giorgio.calderone@inaf.it.

Table 3. CCA transformation matrix for the magnitude band combination in the largest sub-sample (covering 43% of the main sample).

Band	Paper I	This work
G (Gaia)	-9.652	-10.02
BP (Gaia)	-4.571	-3.680
RP (Gaia)	+10.21	+9.332
g (Skymapper)	+2.297	+2.091
r (Skymapper)	+4.637	+4.006
i (Skymapper)	-2.129	-1.386
z (Skymapper)	+3.089	+3.407
J (2MASS)	-0.8026	-0.7531
H (2MASS)	+3.733	+3.984
K (2MASS)	+0.458	+0.5796
W1 (WISE)	-8.250	-7.629
W2 (WISE)	+0.263	-0.7174
W3 (WISE)	+2.348	+2.326
log G (Gaia)	+142.9	+149.4
log BP (Gaia)	+72.69	+57.33
log RP (Gaia)	-138.6	-125.4
log g (Skymapper)	-40.05	-36.85
log r (Skymapper)	-71.36	-61.19
log i (Skymapper)	+33.78	+22.85
log z (Skymapper)	-45.00	-49.95
log J (2MASS)	+14.76	+13.89
log H (2MASS)	-50.95	-53.82
log K (2MASS)	-8.637	-10.47
log W1 (WISE)	+141.7	+132.2
log W2 (WISE)	-22.17	-6.822
log W3 (WISE)	-41.23	-40.81
offset	+10.45	+5.014

Bianchi, L., Shiao, B., & Thilker, D. 2017, ApJS, 230, 24, doi: 10.3847/1538-4365/aa7053

Bonvin, V., Courbin, F., Suyu, S. H., et al. 2017, MNRAS, 465, 4914, doi: 10.1093/mnras/stw3006

Calderone, G., Boutsia, K., Cristiani, S., et al. 2019, ApJ, 887, 268, doi: 10.3847/1538-4357/ab510a

Colless, M., Dalton, G., Maddox, S., et al. 2001, MNRAS, 328, 1039, doi: 10.1046/j.1365-8711.2001.04902.x

Cooke, R. J., & Fumagalli, M. 2018, Nature Astronomy, 2, 957, doi: 10.1038/s41550-018-0584-z

Cristiani, S., Serrano, L. M., Fontanot, F., Vanzella, E., & Monaco, P. 2016, MNRAS, 462, 2478, doi: 10.1093/mnras/stw1810

Dai, X., Shankar, F., & Sivakoff, G. R. 2012, ApJ, 757, 180, doi: 10.1088/0004-637X/757/2/180

D'Odorico, V., Cristiani, S., Pomante, E., et al. 2016, MNRAS, 463, 2690, doi: 10.1093/mnras/stw2161

Fan, X., & SDSS Collaboration. 2000, in American Astronomical Society Meeting Abstracts, Vol. 197, American Astronomical Society Meeting Abstracts, 27.01

Fontanot, F., Cristiani, S., Monaco, P., et al. 2007, A&A, 461, 39, doi: 10.1051/0004-6361:20066073

Fontanot, F., De Lucia, G., Hirschmann, M., et al. 2020, arXiv e-prints, arXiv:2002.10576. https://arxiv.org/abs/2002.10576

Gaia Collaboration, Brown, A. G. A., Vallenari, A., et al. 2018, A&A, 616, A1, doi: 10.1051/0004-6361/201833051

Grazian, A., Giallongo, E., Boutsia, K., et al. 2018, A&A, 613, A44, doi: 10.1051/0004-6361/201732385

Hall, P. B., Anderson, S. F., Strauss, M. A., et al. 2002, ApJS, 141, 267, doi: 10.1086/340546

Hazard, C., McMahon, R. G., Webb, J. K., & Morton, D. C. 1987, ApJ, 323, 263, doi: 10.1086/165823

Iršič, V., Viel, M., Haehnelt, M. G., et al. 2017, PhRvD, 96, 023522, doi: 10.1103/PhysRevD.96.023522

Jones, D. H., Read, M. A., Saunders, W., et al. 2009, MNRAS, 399, 683, doi: 10.1111/j.1365-2966.2009.15338.x

Leite, A. C. O., Martins, C. J. A. P., Molaro, P., Corre, D., & Cristiani, S. 2016, PhRvD, 94, 123512, doi: 10.1103/PhysRevD.94.123512

Liske, J., Grazian, A., Vanzella, E., et al. 2008, MNRAS, 386, 1192, doi: 10.1111/j.1365-2966.2008.13090.x

Pâris, I., Petitjean, P., Aubourg, É., et al. 2018, A&A, 613, A51, doi: 10.1051/0004-6361/201732445

Prochaska, J. X., Worseck, G., & O'Meara, J. M. 2009, ApJL, 705, L113, doi: 10.1088/0004-637X/705/2/L113

Romano, M., Grazian, A., Giallongo, E., et al. 2019, A&A, 632, A45, doi: 10.1051/0004-6361/201935550

Sandage, A. 1962, ApJ, 136, 319, doi: 10.1086/147385

Schindler, J.-T., Fan, X., McGreer, I. D., et al. 2019a, ApJ, 871, 258, doi: 10.3847/1538-4357/aaf86c

Schindler, J.-T., Fan, X., Huang, Y.-H., et al. 2019b, ApJS, 243, 5, doi: 10.3847/1538-4365/ab20d0

Skrutskie, M. F., Cutri, R. M., Stiening, R., et al. 2006, AJ, 131, 1163, doi: 10.1086/498708

Tie, S. S., Martini, P., Mudd, D., et al. 2017, AJ, 153, 107, doi: 10.3847/1538-3881/aa5b8d

Valiante, R., Schneider, R., Volonteri, M., & Omukai, K. 2016, MNRAS, 457, 3356, doi: 10.1093/mnras/stw225

Véron-Cetty, M. P., & Véron, P. 2010, A&A, 518, A10, doi: 10.1051/0004-6361/201014188

Wang, F., Wu, X.-B., Fan, X., et al. 2016, ApJ, 819, 24, doi: 10.3847/0004-637X/819/1/24

Webster, R. L., Ferguson, A. M. N., Corrigan, R. T., & Irwin, M. J. 1991, AJ, 102, 1939, doi: 10.1086/116015

Werk, J. K., Prochaska, J. X., Tumlinson, J., et al. 2014, ApJ, 792, 8, doi: 10.1088/0004-637X/792/1/8

Wolf, C., Onken, C. A., Luvaul, L. C., et al. 2018, PASA, 35, e010, doi: 10.1017/pasa.2018.5

Wolf, C., Hon, W. J., Bian, F., et al. 2020, MNRAS, 491, 1970, doi: 10.1093/mnras/stz2955

Worseck, G., Davies, F. B., Hennawi, J. F., & Prochaska, J. X. 2019, ApJ, 875, 111, doi: 10.3847/1538-4357/ab0fa1

Worseck, G., Prochaska, J. X., Hennawi, J. F., & McQuinn, M. 2016, ApJ, 825, 144, doi: 10.3847/0004-637X/825/2/144

Worseck, G., Prochaska, J. X., O'Meara, J. M., et al. 2014, MNRAS, 445, 1745, doi: 10.1093/mnras/stu1827

Wright, E. L., Eisenhardt, P. R. M., Mainzer, A. K., et al. 2010, AJ, 140, 1868, doi: 10.1088/0004-6256/140/6/1868

Wu, X.-B., Hao, G., Jia, Z., Zhang, Y., & Peng, N. 2012, AJ, 144, 49, doi: 10.1088/0004-6256/144/2/49

Wu, X.-B., Wang, F., Fan, X., et al. 2015, Nature, 518, 512, doi: 10.1038/nature14241

Table 4. All observed sources with secure redshift identification

Skymapper ID	R.A. (J2000)	DEC. (J2000)	m_i (mag)	$z_{\rm spec}$	Class	Candidate PaperI	Candidate New	Date-Obs	Inst
107306	21:01:34.72	-30:10:29.75	17.616	2.761	QSO	Y	Y	2019-09	NTT
343536	21:38:41.84	-33:49:37.21	17.660	3.253	QSO	Y	Y	2019-09	NTT
397340[a]	21:57:28.21	-36:02:15.11	17.367	4.771	QSO	Y	Y	2019-08	WFCCD
583628[b]	21:32:25.90	-28:31:33.24	17.605	2.821	QSO	Y	Y	2019-09	NTT
755996	21:30:54.92	-22:46:54.51	17.693	1.749	QSO	Y	N	2019-09	NTT
838086	21:49:28.24	-27:47:46.22	17.114	2.495	QSO	Y	Y	2019-09	NTT
1316873	22:55:26.10	-36:39:33.80	17.531	1.148	QSO	Y	N	2019-09	NTT
1318863	22:52:47.11	-35:42:01.46	17.692	2.630	QSO	Y	Y	2019-09	NTT
1826062	23:01:39.67	-28:59:46.08	17.062	0.000	STAR	Y	N	2019-08	WFCCD
2415223	21:05:01.83	-13:34:40.76	17.514	2.346	QSO	Y	Y	2019-09	NTT
2809723	21:54:54.84	-18:06:03.36	17.690	3.000	QSO	Y	Y	2019-09	NTT
3310797	21:32:17.64	-06:07:50.64	17.732	0.000	STAR	Y	N	2019-09	NTT
3479216	21:19:19.03	-04:56:56.93	16.959	2.672	QSO	Y	Y	2019-09	NTT
3709817	21:40:53.51	-05:56:47.09	17.582	2.001	QSO	Y	Y	2019-09	NTT
4045023	21:55:13.29	-03:16:05.61	17.410	3.690	QSO	Y	Y	2019-08	WFCCD
4342067	22:57:00.78	-21:42:09.66	17.280	2.833	QSO	Y	Y	2019-09	WFCCD
4342686[b]	22:59:39.04	-22:50:34.90	17.709	3.486	QSO	Y	Y	2019-09	NTT
4441259	22:27:54.04	-15:49:38.61	17.379	2.647	QSO	Y	Y	2019-09	NTT
4538557	22:46:46.21	-16:02:41.71	17.547	2.259	QSO	Y	Y	2019-09	NTT
4788903	23:56:40.97	-21:15:56.84	16.764	1.738	QSO	Y	Y	2019-09	NTT
4922910	23:43:15.99	-18:21:12.21	17.617	3.332	QSO	Y	Y	2019-09	NTT
4924968	23:40:28.39	-17:24:46.12	17.609	4.257	QSO	Y	Y	2019-09	NTT
5003358	23:59:21.09	-14:57:22.91	17.705	2.953	QSO	Y	Y	2019-09	NTT
5035730	22:22:41.07	-10:27:09.45	17.613	1.820	QSO	Y	Y	2019-09	NTT
5081975	22:23:13.66	-08:54:16.34	17.593	2.706	QSO	Y	Y	2019-09	NTT
5552633	23:15:12.19	-11:23:43.85	17.704	2.561	QSO	Y	Y	2019-09	NTT
5564557	23:23:46.94	-12:15:03.37	17.599	2.752	QSO	Y	Y	2019-09	NTT
5931917	23:47:49.34	-04:33:32.60	17.679	1.880	QSO	Y	N	2019-12	WFCCD
6009251	00:01:43.86	-44:25:35.10	17.624	2.572	QSO	Y	Y	2019-09	NTT
6146221	00:21:33.83	-37:40:08.04	17.641	2.573	QSO	Y	Y	2019-09	NTT
6232292	01:11:58.59	-40:33:17.64	17.611	3.432	QSO	Y	Y	2019-09	NTT
6419289	00:00:11.42	-33:10:50.86	17.605	3.106	QSO	Y	Y	2019-09	NTT
6427176	00:15:48.69	-34:03:50.83	17.507	0.055	AGN	Y	Y	2019-09	NTT
6810884	01:43:22.60	-25:38:34.27	17.748	2.307	QSO	Y	Y	2019-09	NTT
6932623	02:04:13.26	-32:51:22.80	17.068	3.835	QSO	Y	Y	2019-11	WFCCD
7015154	02:39:54.21	-34:38:36.83	17.911	0.000	STAR	Y	N	2019-09	NTT

Table 4 *continued*

Table 4 *(continued)*

Skymapper ID	R.A. (J2000)	DEC. (J2000)	m_i (mag)	$z_{\rm spec}$	Class	Candidate PaperI	Candidate New	Date-Obs	Inst
7088896	02:49:54.68	-33:48:35.91	16.706	2.712	QSO	Y	Y	2019-09	NTT
7125196	02:44:06.47	-30:07:49.93	17.703	0.063	AGN	Y	Y	2019-09	NTT
7134124	02:57:16.05	-31:26:44.44	17.671	3.599	QSO	Y	Y	2019-09	NTT
7152915	01:51:52.22	-32:52:38.96	17.206	0.196	AGN	Y	N	2019-08	WFCCD
7250804[b]	01:50:41.58	-25:08:46.32	17.603	3.596	QSO	Y	Y	2019-09	NTT
7277955	02:20:23.13	-26:12:40.04	17.405	3.096	QSO	Y	Y	2019-11	LDSS-3
7292553	02:09:46.00	-24:01:11.19	17.679	1.370	QSO	Y	N	2019-09	NTT
7341051	02:44:49.14	-29:04:49.25	17.422	3.240	QSO	Y	Y	2019-11	WFCCD
7560979	00:32:03.76	-21:27:29.73	17.685	1.855	QSO	Y	N	2019-12	WFCCD
7565232[c]	00:39:01.09	-21:44:28.89	17.597	3.027	QSO	Y	Y	2019-09	NTT
7687616	00:39:19.11	-19:06:19.36	17.745	0.852	QSO	Y	Y	2019-09	NTT
7751454	00:44:18.35	-15:04:13.35	17.442	2.755	QSO	Y	Y	2019-08	WFCCD
7829753	01:27:48.47	-23:34:58.12	17.176	2.933	QSO	Y	Y	2019-08	WFCCD
7901686	01:10:02.61	-18:43:20.07	17.561	2.940	QSO	Y	Y	2019-09	NTT
7931324	01:02:53.62	-14:15:22.53	17.482	0.035	GAL	Y	N	2019-08	WFCCD
7957603	01:33:16.52	-17:39:23.61	17.663	2.903	QSO	Y	Y	2019-09	NTT
8145069[b]	00:43:46.84	-11:17:01.77	17.510	3.510	QSO	Y	Y	2019-09	NTT
8170168	00:32:20.84	-08:13:00.92	17.356	2.838	QSO	Y	Y	2019-11	WFCCD
8430815[b]	01:03:18.06	-13:05:09.89	17.242	4.072	QSO	Y	Y	2019-08	WFCCD
8493702[c]	01:20:35.95	-09:46:32.02	17.653	3.009	QSO	Y	Y	2019-09	NTT
8513332	01:34:10.33	-12:16:31.76	17.072	2.010	QSO	Y	N	2019-11	WFCCD
8529305	01:40:41.94	-12:36:22.39	17.587	3.178	QSO	Y	Y	2019-09	NTT
8590857	00:58:33.99	-04:08:23.66	17.393	0.048	AGN	Y	Y	2019-08	WFCCD
8619006[**]	01:00:49.23	-03:19:13.97	17.25	3.45	QSO	Y	?	2018-10	IMACS
8733320	01:37:35.48	-02:46:06.09	17.678	0.048	AGN	Y	Y	2019-09	NTT
8789744[c]	01:55:58.27	-19:28:48.98	17.393	3.655	QSO	Y	Y	2019-08	WFCCD
8795094	02:05:56.09	-19:53:25.57	17.149	0.205	AGN	Y	N	2019-11	LDSS-3
8904188	02:16:41.24	-16:00:18.55	17.748	3.039	QSO	Y	Y	2019-09	NTT
8918253	02:20:15.17	-14:53:54.10	17.664	2.365	QSO	Y	Y	2019-12	LDSS-3
9089958[**]	02:45:43.76	-12:06:03.71	16.672	0.03	GAL	N	?	2018-09	LDSS-3
9177858	02:08:56.49	-09:01:06.21	17.733	2.665	QSO	Y	Y	2019-09	NTT
9250343[c]	01:59:00.68	-03:27:37.18	17.479	2.946	QSO	Y	Y	2019-08	WFCCD
9407358	02:52:26.99	-09:29:18.21	17.063	2.255	QSO	Y	Y	2019-11	WFCCD
9892519	22:44:25.86	+02:10:08.30	17.015	0.060	GAL	Y	N	2019-09	NTT
10476365	03:36:43.14	-32:20:04.22	17.583	0.050	AGN	Y	Y	2019-09	NTT
10531556	04:08:12.64	-34:37:48.67	17.659	3.279	QSO	Y	Y	2020-01	NTT
10572165	03:16:42.30	-28:03:45.07	17.594	2.313	QSO	Y	Y	2019-09	NTT
10719380	03:56:17.49	-32:08:19.87	17.585	2.291	QSO	Y	Y	2019-09	NTT

Table 4 *continued*

Table 4 *(continued)*

Skymapper ID	R.A. (J2000)	DEC. (J2000)	m_i (mag)	$z_{\rm spec}$	Class	Candidate PaperI	Candidate New	Date-Obs	Inst
10748545	03:55:08.17	-30:11:53.97	17.316	0.068	AGN	Y	N	2019-11	WFCCD
10790773	03:49:16.29	-26:55:39.63	17.674	1.938	QSO	Y	N	2019-09	NTT
10798423	03:36:20.00	-24:25:47.32	17.308	0.540	QSO	N	N	2019-12	WFCCD
10830553	03:53:01.84	-25:48:23.05	17.749	3.083	QSO	Y	Y	2019-09	NTT
10875592	04:05:48.52	-24:21:15.18	17.449	2.785	QSO	Y	Y	2019-12	WFCCD
11028492	04:21:11.68	-34:34:03.64	17.537	1.780	QSO	Y	N	2019-11	WFCCD
11053925*	04:40:01.13	-37:55:34.52	18.317	3.852	QSO	-	-	2020-01	NTT
11163743	05:12:15.00	-41:20:13.86	17.616	3.144	QSO	Y	Y	2020-01	NTT
11270169*	05:04:56.56	-39:52:45.03	18.251	3.237	QSO	-	-	2020-01	NTT
11343829	05:31:08.81	-37:48:20.40	17.651	3.170	QSO	Y	Y	2019-11	LDSS-3
11382764	05:51:33.62	-40:56:31.83	17.879	2.819	QSO	Y	Y	2020-01	NTT
11477581	04:23:33.67	-32:54:14.19	17.463	2.270	QSO	Y	Y	2019-12	WFCCD
11513515	04:30:16.02	-31:57:32.97	17.918	3.552	QSO	Y	Y	2020-01	NTT
11530749*	04:42:05.78	-34:46:49.78	18.358	2.959	QSO	-	-	2020-01	NTT
11621558*	04:14:00.70	-27:20:58.62	18.268	3.998	QSO	-	-	2020-01	NTT
11625837*	04:23:28.88	-27:52:23.74	18.166	3.016	QSO	-	-	2020-01	NTT
11639037	04:29:37.15	-28:35:43.10	17.389	2.569	QSO	Y	Y	2019-12	WFCCD
11708647	04:44:10.65	-29:13:07.15	17.476	1.841	QSO	Y	Y	2020-01	NTT
11797890	05:13:04.21	-35:28:51.50	17.397	3.050	QSO	Y	Y	2019-12	WFCCD
11871566*	05:19:04.89	-33:03:27.23	18.031	3.272	QSO	-	-	2020-01	NTT
12020560	05:50:37.14	-32:39:11.73	17.913	3.369	QSO	Y	Y	2020-01	NTT
12185422	05:42:50.82	-31:03:24.12	17.634	2.620	QSO	Y	Y	2019-11	WFCCD
12375861	03:06:13.04	-15:17:46.67	17.329	2.590	QSO	Y	Y	2019-12	WFCCD
12411621	03:19:01.77	-17:07:19.05	17.626	2.526	QSO	Y	Y	2019-09	NTT
12432405	03:07:00.94	-14:04:56.95	17.474	1.670	QSO	Y	Y	2019-12	WFCCD
12455576**	03:03:54.28	-10:50:49.01	16.35	0.04	GAL	N	?	2018-09	LDSS-3
12476780*	03:19:04.82	-13:42:00.18	18.370	2.989	QSO	-	-	2020-01	NTT
12513469	03:29:03.97	-12:05:42.70	17.641	2.614	QSO	Y	Y	2019-09	NTT
12559809	03:42:21.23	-17:55:11.47	17.236	2.033	QSO	Y	Y	2019-11	LDSS-3
12668545	03:41:38.05	-11:42:59.46	17.205	2.800	QSO	Y	Y	2019-12	WFCCD
12750382	04:09:04.91	-13:37:00.61	17.519	2.771	QSO	Y	Y	2020-01	NTT
12817400	03:26:45.28	-08:47:00.54	17.365	2.348	QSO	Y	Y	2019-12	WFCCD
12931253	03:23:14.75	-02:29:58.63	17.881	0.082	GAL	Y	N	2019-09	NTT
12941812	03:25:25.48	-02:18:04.20	17.523	2.268	QSO	Y	N	2019-12	LDSS-3
12957365*	03:31:06.08	-00:32:38.53	16.189	0.000	STAR	-	-	2020-01	LDSS-3
12989144	03:48:51.22	-10:15:53.61	16.974	2.498	QSO	Y	Y	2019-12	WFCCD
13173703*	03:36:34.04	-00:49:16.40	14.678	0.002	GAL	-	-	2020-01	NTT
13291946	04:09:34.40	-02:17:38.04	17.640	3.202	QSO	Y	Y	2020-01	NTT

Table 4 *continued*

Table 4 *(continued)*

Skymapper ID	R.A. (J2000)	DEC. (J2000)	m_i (mag)	$z_{\rm spec}$	Class	Candidate PaperI	Candidate New	Date-Obs	Inst
13323971	04:17:23.77	-21:47:13.67	17.344	2.060	QSO	Y	Y	2019-12	WFCCD
13409036	04:37:47.11	-24:16:23.62	17.239	1.980	QSO	N	N	2019-12	WFCCD
13422105	04:38:56.76	-22:56:53.36	15.949	0.026	GAL	N	N	2019-12	WFCCD
13479091*	04:39:54.55	-19:43:51.32	18.035	2.609	QSO	-	-	2020-01	NTT
13623074	04:40:53.44	-18:43:28.06	17.674	2.832	QSO	Y	Y	2019-11	LDSS-3
13754735	05:04:50.03	-24:32:51.42	17.488	1.789	QSO	Y	Y	2019-12	LDSS-3
14047570	05:37:28.45	-21:56:10.42	17.125	2.835	QSO	Y	Y	2019-12	WFCCD
14148404	05:14:11.75	-19:01:39.46	17.681	2.609	QSO	Y	Y	2019-11	WFCCD
14203137	05:24:38.81	-18:16:04.14	16.831	1.969	QSO	Y	Y	2019-12	WFCCD
14271415	05:25:49.05	-16:16:12.37	17.843	3.567	QSO	Y	Y	2020-01	NTT
14661311	04:50:19.69	-11:18:36.99	17.394	2.560	QSO	Y	Y	2019-12	WFCCD
14756860*	05:03:29.07	-09:41:52.22	18.389	3.307	QSO	-	-	2020-01	NTT
14797495[c]	04:25:03.70	-05:45:08.94	17.498	3.040	QSO	Y	Y	2019-11	WFCCD
14832947	04:32:49.02	-05:41:48.21	17.600	0.165	AGN	Y	N	2019-11	LDSS-3
14921486	04:32:50.36	-01:12:53.72	16.690	1.691	QSO	Y	N	2019-09	NTT
14930439[c]	04:36:23.92	-00:04:02.89	17.404	3.852	QSO	Y	Y	2020-01	NTT
15015396	04:58:13.47	-03:52:51.60	17.375	3.000	QSO	Y	Y	2019-12	WFCCD
15040824	04:46:17.76	-02:20:15.64	17.687	2.533	QSO	Y	Y	2019-11	LDSS-3
15088950*	05:02:54.73	-03:09:23.73	18.089	3.689	QSO	-	-	2020-01	NTT
15248403	05:07:32.14	-06:58:02.27	17.427	2.960	QSO	Y	Y	2019-12	WFCCD
16164525*	06:01:37.14	-43:41:43.80	18.378	3.499	QSO	-	-	2020-01	NTT
16539422	06:02:18.73	-36:59:24.72	17.518	2.920	QSO	Y	N	2019-11	WFCCD
47669241*	08:15:45.64	-01:38:18.59	16.261	0.000	STAR	-	-	2020-01	LDSS-3
48196484*	08:58:49.38	-02:34:05.48	16.381	0.000	STAR	-	-	2020-01	LDSS-3
48449084*	08:44:22.01	+04:32:44.27	18.036	3.327	QSO	-	-	2020-01	NTT
51718111*	10:07:03.55	-23:57:13.36	18.287	3.347	QSO	-	-	2020-01	NTT
54192246	10:59:56.17	-30:28:27.95	17.487	2.610	QSO	Y	Y	2020-01/02	NTT/LDSS-3
54298405	10:58:09.30	-26:05:42.29	17.505	2.876	QSO	Y	Y	2020-01	NTT
54680559[a]	11:10:54.68	-30:11:29.88	17.346	4.779	QSO	Y	Y	2020-01	NTT
55462080	09:30:53.18	-12:12:29.67	17.007	0.000	STAR	Y	N	2020-02	LDSS-3
55582991	09:49:02.92	-20:07:23.36	16.298	1.866	QSO	N	N	2020-02	LDSS-3
55799640	09:44:35.17	-16:16:32.31	17.224	2.897	QSO	Y	Y	2020-02	LDSS-3
56003412	10:12:57.45	-14:34:12.40	17.540	3.229	QSO	Y	Y	2020-01	NTT
56507631*	09:49:34.23	-08:03:08.77	18.086	2.333	QSO	-	-	2020-01	NTT
56610095	09:59:20.61	-06:47:25.66	17.189	1.797	QSO	Y	Y	2020-02	LDSS-3
56626491	10:04:16.57	-07:46:34.72	17.327	0.558	QSO	Y	N	2020-01	NTT
56648626	09:40:52.85	-05:09:32.44	17.144	2.370	QSO	Y	Y	2020-02	LDSS-3
56660065	09:41:19.36	-04:08:12.54	16.754	0.000	STAR	Y	N	2020-01	LDSS-3

Table 4 *continued*

Table 4 *(continued)*

Skymapper ID	R.A. (J2000)	DEC. (J2000)	m_i (mag)	$z_{\rm spec}$	Class	Candidate PaperI	Candidate New	Date-Obs	Inst
56681692	09:43:51.97	-03:21:02.73	17.464	1.701	QSO	N	N	2020-02	LDSS-3
56699168*	09:37:47.61	-02:01:26.30	16.610	0.000	STAR	-	-	2020-01	LDSS-3
56749347	09:52:29.66	-04:08:02.85	17.487	2.074	QSO	Y	Y	2020-01	LDSS-3
56791679*	09:54:32.83	-02:07:51.29	16.369	0.000	STAR	-	-	2020-01	LDSS-3
56823181*	10:12:05.23	-02:15:24.61	16.358	0.000	STAR	-	-	2020-01	LDSS-3
56933068	10:25:07.94	-20:58:19.50	17.152	2.308	QSO	Y	Y	2020-02	LDSS-3
57291610*	10:32:52.81	-13:52:04.59	18.098	2.950	QSO	-	-	2020-01	NTT
57292353	10:35:25.96	-14:39:47.44	17.298	2.888	QSO	Y	Y	2020-01	NTT
57466047	11:13:57.01	-26:04:58.35	16.817	2.949	QSO	Y	Y	2020-01/02	NTT/LDSS-3
57669548*	11:34:40.56	-21:03:22.78	16.205	2.774	QSO	-	-	2020-01	NTT
58115878*	10:54:45.47	-10:53:29.52	18.053	0.156	GAL	-	-	2020-01	LDSS-3
58723356	11:13:32.47	-03:09:13.98	17.949	3.731	QSO	Y	Y	2020-01	NTT
58823120*	11:57:43.62	-06:50:04.73	18.247	2.748	QSO	-	-	2020-01	NTT
60288193	13:04:42.64	-36:04:27.43	17.892	0.155	AGN	Y	N	2020-01	NTT
61068064	12:41:46.38	-29:34:49.05	17.404	3.048	QSO	Y	Y	2020-01	NTT
62209153	13:55:44.05	-35:08:15.11	17.447	0.000	STAR	Y	N	2020-01	NTT
63230995[b]	14:08:01.83	-27:58:20.34	17.641	4.447	QSO	Y	Y	2020-01	NTT
63285615	13:49:40.58	-26:33:42.92	17.222	3.023	QSO	Y	Y	2020-01	NTT
63739700	14:32:28.52	-24:44:35.07	17.357	2.718	QSO	Y	Y	2020-01	NTT
63982611	12:15:37.66	-24:53:23.63	17.043	0.083	GAL	N	N	2020-01	NTT
64116716	12:49:08.53	-25:32:38.86	17.437	0.147	AGN	N	N	2020-01	LDSS-3
65072412	12:27:24.77	-11:33:35.05	14.951	0.000	STAR	N	N	2020-01	NTT
65723003*	13:20:01.62	-06:53:21.60	18.188	1.329	QSO	-	-	2020-01	NTT
65842041*	13:45:17.91	-08:29:57.17	18.254	0.472	AGN	-	-	2020-01	NTT
98859792	15:43:22.37	-19:42:41.10	16.004	0.177	AGN	Y	N	2019-08	WFCCD
125383528	19:40:12.00	-41:18:22.33	17.642	2.618	QSO	Y	Y	2019-09	NTT
135055221	20:06:00.80	-39:37:32.61	17.623	1.340	QSO	Y	N	2019-09	NTT
135169820	20:19:01.86	-38:27:21.89	17.387	2.070	QSO	Y	N	2019-08	WFCCD
135210414	20:20:27.08	-36:34:25.79	17.214	0.086	AGN	Y	N	2019-09	NTT
135463347	20:13:23.96	-33:47:50.43	16.767	2.745	QSO	Y	Y	2019-09	NTT
135639174	20:46:44.37	-33:36:06.31	17.725	0.132	AGN	Y	N	2019-09	NTT
135758989	20:51:59.18	-32:28:38.67	17.577	1.974	QSO	Y	Y	2019-09	NTT
136204383	20:16:19.21	-27:33:21.66	17.458	2.062	QSO	Y	N	2019-09	NTT
136230878	20:19:46.01	-27:40:16.20	17.653	0.025	AGN	Y	Y	2019-09	NTT
136588662[b]	20:11:58.77	-26:23:40.86	17.662	3.657	QSO	Y	Y	2019-09	NTT
136973888	20:55:54.12	-24:56:25.25	17.384	0.126	AGN	Y	N	2019-09	NTT
137044597	20:39:21.61	-24:00:05.00	17.942	2.916	QSO	Y	Y	2019-09	NTT
137166249[b]	20:48:48.28	-22:51:52.07	17.449	3.100	QSO	Y	Y	2019-08	WFCCD

Table 4 *continued*

Table 4 *(continued)*

Skymapper ID	R.A. (J2000)	DEC. (J2000)	m_i (mag)	$z_{\rm spec}$	Class	Candidate PaperI	Candidate New	Date-Obs	Inst
137203486	20:49:49.03	-21:46:33.63	17.299	0.038	AGN	Y	N	2019-09	NTT
171528002	20:19:31.38	-16:34:40.04	17.328	2.619	QSO	Y	Y	2019-09	NTT
172129292	20:40:43.96	-15:26:26.78	17.666	0.119	AGN	Y	N	2019-09	NTT
175467261	20:44:24.99	-01:48:55.56	17.335	2.304	QSO	Y	Y	2019-09	NTT
288304909	06:56:21.64	-74:21:02.00	17.359	2.116	QSO	Y	Y	2019-12	WFCCD
288408065	06:53:54.47	-75:07:56.30	17.339	3.081	QSO	Y	Y	2020-01	NTT/LDSS-3
288742885	06:45:57.00	-67:53:09.09	17.720	4.314	QSO	Y	Y	2020-01	NTT
293711383*	06:20:07.34	-61:55:57.93	18.021	3.320	QSO	-	-	2020-01	NTT
293925557	06:12:19.16	-55:44:21.29	17.298	2.285	QSO	Y	Y	2019-12	WFCCD
293946915*	06:18:13.16	-55:19:46.12	18.049	3.117	QSO	-	-	2020-01	NTT
293970104*	06:06:20.93	-54:19:38.59	18.210	3.343	QSO	-	-	2020-01	NTT
294463461	06:18:46.36	-51:08:16.66	17.173	2.050	QSO	Y	Y	2019-12	WFCCD
300818220	19:18:53.50	-52:50:11.91	17.311	2.022	QSO	Y	Y	2019-08	WFCCD
301296617	20:07:39.92	-58:10:37.65	17.744	3.289	QSO	Y	Y	2019-09	NTT
301508731	20:18:27.87	-51:51:00.35	17.060	2.639	QSO	Y	Y	2019-09	NTT
301643566	20:24:13.87	-53:12:13.87	16.962	2.208	QSO	Y	Y	2019-09	NTT
301677762	20:35:33.65	-52:53:29.14	17.746	2.572	QSO	Y	Y	2019-09	NTT
302676587	18:59:46.16	-74:34:32.82	17.310	0.142	AGN	Y	N	2019-09	NTT
303302739	20:12:29.32	-67:32:16.66	17.056	2.512	QSO	Y	N	2019-09	NTT
303604203	18:55:09.84	-81:38:28.84	17.456	1.746	QSO	Y	N	2019-09	NTT
304156429	20:25:23.01	-73:01:18.98	16.695	0.097	AGN	Y	N	2019-08	WFCCD
304169254	20:35:30.89	-75:38:11.99	17.705	2.195	QSO	Y	Y	2019-09	NTT
304191239	20:36:26.11	-78:16:34.13	17.031	2.627	QSO	Y	Y	2019-09	NTT
304867318	20:35:17.07	-62:37:01.82	16.730	2.709	QSO	Y	N	2019-09	NTT
305094211	21:10:38.23	-66:38:43.85	17.369	0.124	AGN	Y	Y	2019-09	NTT
305139405	21:32:46.07	-65:20:42.57	17.233	2.206	QSO	Y	Y	2019-08	WFCCD
305149856	20:36:41.07	-58:37:01.26	17.620	1.701	QSO	Y	Y	2019-09	NTT
305336573	21:08:17.67	-62:17:57.53	17.589	3.794	QSO	Y	Y	2019-09	NTT
305446236	21:40:40.86	-58:51:21.57	17.325	3.021	QSO	Y	Y	2019-09	NTT
305565087	21:57:46.57	-72:31:14.44	17.329	2.908	QSO	Y	Y	2019-09	NTT
305588367	21:58:49.70	-70:35:52.25	17.121	0.218	AGN	Y	N	2019-08	WFCCD
305669171	22:20:57.18	-69:59:23.17	17.432	2.221	QSO	Y	Y	2019-09	NTT
305744092	22:54:00.77	-72:07:48.71	17.584	2.922	QSO	Y	Y	2019-09	NTT
305772027	23:21:14.00	-73:26:02.07	17.103	0.143	AGN	Y	N	2019-08	WFCCD
305790724	22:34:32.52	-71:22:42.90	17.319	1.932	QSO	Y	N	2019-12	WFCCD
305817005	22:53:01.59	-69:38:13.41	17.725	3.082	QSO	Y	Y	2019-09	NTT
306048062	22:58:05.07	-65:59:07.40	17.712	2.796	QSO	Y	Y	2019-09	NTT
306142589	23:56:05.44	-66:09:49.56	17.622	3.143	QSO	Y	Y	2019-09	NTT

Table 4 *continued*

Table 4 *(continued)*

Skymapper ID	R.A. (J2000)	DEC. (J2000)	m_i (mag)	$z_{\rm spec}$	Class	Candidate PaperI	Candidate New	Date-Obs	Inst
306255584	20:02:54.69	-42:14:21.06	17.516	2.612	QSO	Y	Y	2019-09	NTT
306376125**	20:18:47.29	-45:46:48.42	16.462	1.355	QSO	Y	N	2019-06	LDSS-3/FIRE
306578934	20:40:01.98	-44:36:33.59	17.571	2.691	QSO	Y	Y	2019-09	NTT
306624073	20:46:36.95	-43:11:40.92	16.303	2.169	QSO	Y	Y	2019-09	NTT
306630517	20:46:33.08	-42:39:02.11	17.692	3.260	QSO	Y	Y	2019-09	NTT
306874313	21:01:47.82	-48:46:23.52	17.527	2.601	QSO	Y	Y	2019-09	NTT
307049678	21:18:23.60	-49:21:16.77	17.735	1.214	QSO	Y	N	2019-09	NTT
307108556	21:37:31.37	-47:38:03.44	16.769	2.448	QSO	Y	Y	2019-09	NTT
307443251	21:25:18.39	-42:05:47.62	17.363	3.549	QSO	Y	Y	2019-09	NTT
307536920	21:51:37.44	-44:36:44.17	17.363	3.638	QSO	Y	Y	2019-09	WFCCD
307772847	21:20:11.80	-53:04:07.41	17.556	2.245	QSO	Y	Y	2019-09	NTT
308002829	21:41:07.72	-52:30:39.28	17.287	2.334	QSO	Y	Y	2019-09	NTT
308038519	21:49:56.64	-50:31:28.72	17.743	3.296	QSO	Y	Y	2019-09	NTT
308280154	23:03:18.38	-59:15:33.20	17.554	1.408	QSO	Y	N	2019-12	LDSS-3
308304837	23:17:51.93	-61:45:57.30	17.136	2.940	QSO	Y	Y	2019-08	WFCCD
308375290[a]	23:35:05.86	-59:01:03.33	17.599	4.540	QSO	Y	Y	2019-09	NTT
308396429	23:44:05.92	-57:57:14.73	17.609	3.177	QSO	Y	Y	2019-09	NTT
308690703	22:41:31.39	-49:40:56.67	17.672	2.764	QSO	Y	Y	2019-09	NTT
308973148	23:44:57.76	-50:14:42.87	17.433	2.343	QSO	Y	Y	2019-12	LDSS-3
308998359	22:58:55.77	-46:41:44.62	17.660	1.899	QSO	Y	N	2019-11	LDSS-3
309030850	23:04:14.36	-44:23:17.76	17.679	2.283	QSO	Y	Y	2019-09	NTT
309431269	05:01:14.50	-80:19:03.28	17.936	2.663	QSO	Y	Y	2020-01	NTT
309455748	05:35:46.75	-78:15:08.61	17.685	2.939	QSO	Y	Y	2019-11	LDSS-3
309656787	01:08:40.41	-82:17:47.76	17.579	2.707	QSO	Y	Y	2019-09	NTT
309939096	03:54:32.05	-74:03:44.86	17.510	0.000	STAR	Y	N	2019-09	NTT
309972073	02:18:10.04	-75:39:43.01	17.699	0.000	STAR	Y	N	2019-09	NTT
310047722	02:50:56.99	-72:04:58.62	17.602	2.892	QSO	Y	Y	2019-09	NTT
310206031	05:09:43.13	-74:09:47.89	17.575	3.773	QSO	Y	Y	2020-01	NTT
311228175	04:31:45.85	-74:51:26.83	17.189	3.140	QSO	Y	Y	2019-12	WFCCD
312716357	05:34:58.75	-64:49:36.83	17.541	3.247	QSO	Y	Y	2020-01	NTT
313912389	04:39:23.74	-65:36:22.83	17.805	3.399	QSO	Y	Y	2020-01	NTT
313928581	04:20:32.51	-66:09:30.84	17.260	2.700	QSO	Y	Y	2019-12	WFCCD
314899504	02:24:11.35	-70:36:38.67	17.739	2.829	QSO	Y	Y	2019-09	NTT
315156166	01:24:25.20	-66:08:13.38	17.554	2.365	QSO	Y	N	2019-12	LDSS-3
315316671	02:43:04.74	-66:23:11.69	17.649	2.055	QSO	Y	Y	2019-09	NTT
315435952	03:12:32.49	-62:38:59.70	16.845	3.016	QSO	Y	Y	2019-09	NTT
315483506	02:24:56.71	-63:31:04.98	17.716	2.706	QSO	Y	Y	2019-09	NTT
315552288	02:37:48.15	-59:59:51.14	17.695	2.756	QSO	Y	Y	2019-09	NTT

Table 4 *continued*

Table 4 *(continued)*

Skymapper ID	R.A. (J2000)	DEC. (J2000)	m_i (mag)	$z_{\rm spec}$	Class	Candidate PaperI	Candidate New	Date-Obs	Inst
315607762	03:17:24.89	-57:36:19.01	17.922	3.844	QSO	Y	Y	2020-01	NTT
315783093	05:47:55.85	-58:40:37.81	17.430	0.000	STAR	N	N	2019-12	WFCCD
315809832	05:27:04.37	-61:54:57.45	16.949	1.879	QSO	Y	Y	2019-12	WFCCD
315974502	05:34:49.40	-57:47:26.92	17.085	2.880	QSO	Y	Y	2019-12	WFCCD
316155633	05:08:24.66	-55:44:40.37	17.979	2.466	QSO	Y	Y	2020-01	NTT
316186672	05:01:00.45	-54:26:49.97	17.093	2.600	QSO	Y	Y	2019-12	WFCCD
316292063	05:48:03.20	-48:48:13.19	16.886	4.147	QSO	Y	Y	2019-12	WFCCD
316293416	05:45:02.05	-49:24:47.35	17.344	2.928	QSO	Y	Y	2020-02	LDSS-3
316383429	05:55:08.16	-45:58:23.61	17.649	3.262	QSO	Y	Y	2020-01	NTT
316434053	05:39:21.91	-45:16:58.03	17.064	2.556	QSO	Y	Y	2019-12	WFCCD
316563116*	05:20:23.95	-47:52:12.06	18.362	3.825	QSO	-	-	2020-01	NTT
316567405*	05:24:10.76	-47:15:28.25	18.052	2.399	QSO	-	-	2020-01	NTT
316591563	05:29:14.28	-45:08:07.03	17.661	3.690	QSO	Y	Y	2020-01	NTT
316663640	04:30:07.62	-56:47:36.38	17.154	3.130	QSO	Y	Y	2019-12	WFCCD
316757721	04:33:26.90	-52:07:58.20	17.777	3.442	QSO	Y	Y	2020-01	NTT
316769552	04:18:15.82	-52:58:14.21	15.171	0.000	STAR	N	N	2019-12	WFCCD
316788893	04:25:40.68	-50:43:15.05	17.528	0.047	AGN	Y	Y	2019-11	WFCCD
316791881	04:11:46.66	-52:12:07.74	17.605	2.022	QSO	Y	Y	2019-11	LDSS-3
316933237	03:45:05.36	-49:35:14.61	17.656	0.000	STAR	Y	N	2019-09	NTT
317020875	04:45:18.99	-46:00:49.84	17.423	2.184	QSO	Y	Y	2019-12	WFCCD
317068530	04:14:59.70	-49:07:56.59	17.652	2.790	QSO	Y	Y	2019-11	LDSS-3
317105305	03:56:39.60	-47:08:34.05	17.407	2.110	QSO	Y	Y	2019-12	WFCCD
317138695	04:30:48.53	-43:28:35.18	17.660	2.757	QSO	Y	Y	2020-01	NTT
317201391	00:42:44.49	-62:41:09.29	17.464	2.055	QSO	Y	N	2019-12	LDSS-3
317253125	00:48:05.34	-59:29:09.44	17.536	3.607	QSO	Y	Y	2019-09	NTT
317343050	01:27:16.87	-58:02:47.28	17.772	3.918	QSO	Y	Y	2020-01	NTT
317358346[a]	00:07:36.56	-57:01:51.73	17.240	4.260	QSO	Y	Y	2019-08	WFCCD
317411112	00:18:30.46	-53:35:35.20	17.744	3.738	QSO	Y	Y	2019-09	NTT
317506585	01:42:17.55	-59:37:00.86	17.717	3.432	QSO	Y	Y	2019-09	NTT
317647507	01:40:04.35	-54:23:15.53	17.623	2.458	QSO	Y	Y	2019-09	NTT
317802750[a]	00:12:24.99	-48:48:29.86	17.715	4.621	QSO	Y	Y	2019-09	NTT
318357314	03:45:42.68	-47:36:31.41	17.590	2.878	QSO	Y	Y	2019-09	NTT
318395533	03:45:07.90	-44:32:44.08	17.192	2.140	QSO	Y	N	2019-12	WFCCD
318397429	03:43:30.07	-43:44:29.86	17.121	1.777	QSO	Y	Y	2019-12	WFCCD
318432798	03:54:35.83	-42:16:30.70	16.737	1.983	QSO	Y	N	2019-12	WFCCD
318446298	03:23:24.22	-44:03:46.17	17.473	2.074	QSO	Y	Y	2020-01	NTT
318479392	03:18:24.60	-41:32:40.30	17.647	2.495	QSO	Y	Y	2019-11	WFCCD
318495154	03:38:35.49	-40:30:41.39	17.309	2.900	QSO	Y	Y	2019-12	WFCCD

Table 4 *continued*

Table 4 *(continued)*

Skymapper ID	R.A. (J2000)	DEC. (J2000)	m_i (mag)	$z_{\rm spec}$	Class	Candidate PaperI	Candidate New	Date-Obs	Inst
318699655	03:21:50.82	-39:53:14.75	17.471	2.794	QSO	Y	Y	2019-12	WFCCD

NOTE—
[a]Independently discovered also by Wolf et al. (2020)
[b]Included also in Schindler et al. (2019b)
[c]Included also in Schindler et al. (2019a)
* Not part of the Main Sample
** after updated reduction of PaperI observed sources